

## Gravity-driven thermoviscous liquid film down a heated or cooled vertical cylinder

Sana Khanum<sup>1</sup> and Naveen Tiwari<sup>2,\*</sup>

<sup>1</sup>*Department of Chemical Engineering, Purdue University, Indiana 47907-2100, USA*

<sup>2</sup>*Department of Chemical Engineering, Indian Institute of Technology Kanpur, Kanpur, Uttar Pradesh 208016, India*

 (Received 20 May 2020; accepted 11 August 2020; published 18 September 2020)

Stability analysis of gravity-driven flow of a thermoviscous liquid on the exterior surface of a uniformly heated or cooled vertical cylinder is presented. The film evolution model derived using lubrication approximation consists of four dimensionless groups, namely, Marangoni number, Biot number, Bond number, and thermoviscosity number. The viscosity of the liquid is modeled as an exponentially varying function of temperature. The thermocapillary stress significantly affects the Rayleigh-Plateau instability for flow over a nonisothermal cylinder with intricate dependence on various parameters involved. For the temporally unstable system, spatiotemporal stability analysis is performed to delineate the parameter regions for convectively and absolutely unstable systems. Brigg's criterion is employed and the critical value of a composite parameter  $\beta$  is evaluated to study the transition from convective to absolute instability. A proper rescaling of the dispersion relation shows that the condition on the composite parameter is  $\beta < 1.507$  for the existence of absolute instability, which is consistent with an earlier work on isothermal flows. Further, an expression is found for the critical composite Marangoni number beyond which the film is always absolutely unstable independent of the Bond number. This critical value is shown to be an increasing function of thermoviscosity number. Results from the nonlinear simulations are in agreement with the predictions of the linear temporal and spatiotemporal analyses.

DOI: [10.1103/PhysRevFluids.5.094005](https://doi.org/10.1103/PhysRevFluids.5.094005)

### I. INTRODUCTION

The dynamics of a thin liquid film flowing down a vertical cylinder under the influence of gravity has been studied extensively due to its wide applications [1–3], including patterning cylindrical surfaces [4], cooling optical fibers [5], and condensing vapor on heat pipes [6]. This system of thin film flow exhibits complex and interesting dynamics due to the stabilizing and destabilizing roles of the axial and azimuthal film curvatures, respectively [7], leading to the formation of droplets and traveling wave patterns [8,9]. Motivated by the experimental work by Quéré [8] on the film instability on vertical fibers, several authors [10–13] have investigated the evolution of film interface into undulating surface leading to traveling waves and droplets.

Coating flows over a heated or cooled cylindrical surface is an essential component of technological applications. In such processes, a nonuniformity in the film profile leads to temperature gradients at the liquid-air interface. It has been shown earlier that for a film on the exterior or interior of a heated cylinder, the interfacial thermal gradients generate the unbalanced thermocapillary stress that has a destabilizing effect on the film [14–16]. For various applications, the viscosity of the liquid may also vary with temperature, and can affect the dynamics of the film. The thermoviscous liquid

---

\*Corresponding author: [naveent@iitk.ac.in](mailto:naveent@iitk.ac.in)

film flow over a flat plate has been studied earlier [17,18]. Coating and rimming flows have also been studied for thermoviscous liquids. [19,20]

Temporal stability analysis of a thin-film flowing down a vertical cylinder for viscous fluids has been explored in various studies [10,12,21,22]. The existence of absolute and convective instabilities in thin-film flow down a vertical cylinder was first examined in detail, both experimentally and theoretically, by Duprat *et al.* [23]. For sufficiently thin films, they found critical condition using long-wave approximation, below which the flow was absolutely unstable. Experimentally they found that for a thicker film or when the drops formed due to the instability assume the same order as the fiber radius, this critical condition gets modified and can be captured using the model of Kliakhandler, Davis, and Bankoff [21]. In their experiments, noise was introduced near the inlet, and the formation of a regular wavy regime was considered as the absolute instability and used to validate the critical condition found theoretically. Camassa *et al.* [24] studied the stability of a gravity film flow in the interior of a tube. In the case of flow in the interior of a tube, the film instability can grow large, leading to choking of the tube. Using the long-wave asymptotic model, they were able to predict the formation of the liquid plug and transition between absolute and convective type instabilities, which was also validated using experiments. Stability analysis of gravity-driven viscous film coating on the interior surface of a heated vertical tube was presented by Ding *et al.* [25]. They demonstrated that the thermocapillary stress (also referred to as the Marangoni stress) was able to generate absolute instability even for sufficiently thin film. Using direct numerical simulations, they showed that the film had more tendency to rupture or breakup into droplets in the absolute instability parametric regime.

The present work is focused on the study of dynamics and stability of a gravity-driven thermoviscous film flowing down the exterior surface of a heated or cooled vertical cylinder in the limit of lubrication approximation, wherein the thickness of the film is assumed to be much smaller than the cylinder radius. Temporal stability analysis is carried out to investigate the stability of the film to small perturbations in Sec. IV. Nonlinear simulations of the derived interfacial film profile subject to initial sinusoidal disturbance are performed, and the results are compared with the growth rates found from the linear theory in Sec. V. Further, the nature of instability is determined by accomplishing spatiotemporal stability analysis and is discussed in Sec. VI. Nonlinear simulations subject to initial Gaussian disturbance are implemented in Sec. VII to study the spatiotemporal dynamics of the flow and the linear spatiotemporal properties are deduced from the nonlinear simulations. Discussions are presented in Sec. VIII followed by the conclusions in Sec. IX.

## II. PROBLEM FORMULATION

Consider an axisymmetric flow of a thin film of liquid with density  $\rho$ , temperature-dependent viscosity  $\mu$ , and surface tension  $\gamma$  flowing down due to gravity on the outside surface of a vertical cylinder of radius  $R$ . The thickness of the film is considered to be much smaller than the radius of the cylinder in this work. The cylinder wall temperature is uniform and maintained at constant surface temperature,  $T_s$ , which, in general, is not equal to the ambient temperature,  $T_\infty$ . The film flows along the  $z$  direction, and  $r$  is the radial direction pointing normal to the surface of the cylinder surface, as shown in Fig. 1. The velocity  $\mathbf{v}$  and pressure  $p$  are governed by the Navier-Stokes equation and the continuity equation for the incompressible flow,

$$\nabla \cdot \mathbf{v} = 0, \quad (1)$$

$$\rho \frac{\partial \mathbf{v}}{\partial t} + \rho \mathbf{v} \cdot \nabla \mathbf{v} = -\nabla p + \nabla \cdot (\mu \nabla \mathbf{v}) + \rho \mathbf{g}, \quad (2)$$

where  $\mathbf{v} = u_r \hat{\mathbf{r}} + u_z \hat{\mathbf{z}}$  with  $u_r$  and  $u_z$  being the radial and axial components of the velocity vector, respectively. Temperature distribution,  $T(r, z, t)$ , across the film is determined by the energy balance

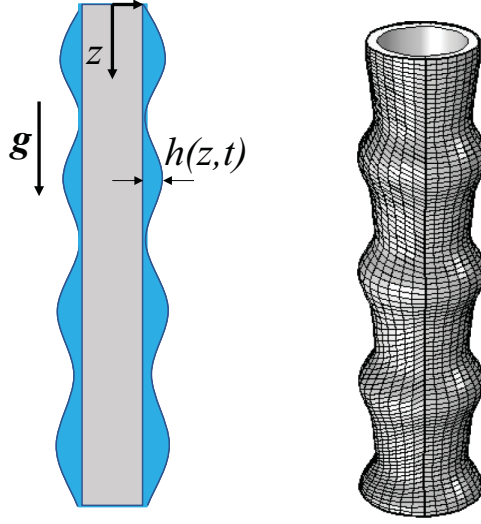


FIG. 1. Schematic of the flow geometry: sectional and three-dimensional views of the cylindrical geometry.

equation

$$\frac{\partial T}{\partial t} + \mathbf{v} \cdot \nabla T = \alpha \nabla^2 T, \quad (3)$$

where  $\alpha = k_{\text{th}}/\rho c_p$  is the thermal diffusivity of the liquid and,  $c_p$  and  $k_{\text{th}}$  represent the specific heat capacity and thermal conductivity of the liquid, respectively.

The widely used exponential viscosity model [26] is employed for a thermoviscous fluid,

$$\mu = \mu_0 \exp \left[ \frac{-\lambda(T - T_s)}{\mu_0} \right], \quad (4)$$

which satisfies  $\mu = \mu_0$  and  $\lambda = -d\mu/dT$  when  $T = T_s$ , where  $\lambda$  is a positive constant ( $\lambda > 0$ ).

An appropriate nondimensional thermoviscosity number  $V$  is defined to quantify the effect of viscosity variation with temperature

$$V = \frac{\lambda \Delta T}{\mu_0}, \quad (5)$$

where  $\Delta T = (T_s - T_\infty)$  is positive for the heated ( $T_s > T_\infty$ ) and negative for the cooled ( $T_s < T_\infty$ ) cylinder surface. As  $V$  is proportional to  $\Delta T$ , they assume the same sign. The surface tension  $\gamma$  is assumed to vary linearly with temperature as

$$\gamma(T) = \gamma_0 + \gamma_T(T - T_\infty), \quad (6)$$

where  $\gamma_0$  is the surface tension of the liquid at the ambient temperature  $T_\infty$  and  $\gamma_T = d\gamma/dT < 0$ , which is true for most of the liquids.

The no-slip and no-penetration boundary conditions are applied at  $r = R$  (surface of the cylinder)

$$u_r = 0, \quad (7)$$

$$u_z = 0. \quad (8)$$

At the liquid-air interface, the normal and tangential stress balance conditions are imposed

$$-p + \mathbf{n} \cdot \boldsymbol{\tau} \cdot \mathbf{n} = -\gamma \nabla_s \cdot \mathbf{n}, \quad (9)$$

$$\mathbf{t} \cdot \boldsymbol{\tau} \cdot \mathbf{n} = \mathbf{t} \cdot \nabla_s \gamma, \quad (10)$$

where  $\boldsymbol{\tau}$  is the viscous stress tensor,  $\mathbf{t}$  is the tangential vector to the free surface,  $\nabla_s = (\mathbf{I} - \mathbf{nn}) \cdot \nabla$  is the surface gradient operator and  $\mathbf{I}$  is the identity tensor.

The boundary conditions for the energy equation are the constant temperature at the surface of the cylinder, i.e., at  $r = R$ ,

$$T = T_s, \quad (11)$$

and the convective cooling at the liquid-air interface, i.e., at  $r = R + h(z, t)$ ,

$$-k_{th} \nabla T^i \cdot \mathbf{n} = h_f (T^i - T_\infty), \quad (12)$$

where  $h_f$  is the film heat transfer coefficient, and  $T^i$  is the interfacial temperature.

The kinematic boundary condition at the free surface,  $r = R + h(z, t)$ , is

$$\frac{\partial h}{\partial t} + u_z \frac{\partial h}{\partial z} = u_r. \quad (13)$$

### A. Lubrication approximation

The variables are nondimensionalized using the following scales:

$$\begin{aligned} \tilde{r} &= \frac{r}{R}, \quad \tilde{z} = \frac{z}{R}, \quad \tilde{t} = \frac{t \rho g H_0^2}{R \mu_0}, \quad \tilde{u}_z = \frac{u_z}{\rho g H_0^2 / \mu_0}, \\ \tilde{u}_r &= \frac{u_r}{\varepsilon \rho g H_0^2 / \mu_0}, \quad \tilde{p} = \frac{p}{\rho g R}, \quad \tilde{T} = \frac{T - T_\infty}{T_s - T_\infty}, \end{aligned} \quad (14)$$

where  $H_0$  is the average film thickness, and  $\varepsilon = H_0/R (\ll 1)$  is an aspect ratio. Further, a new radial coordinate  $\tilde{y} = (\tilde{r} - 1)/\varepsilon$  is introduced, and the governing equations and boundary conditions discussed above are nondimensionalized in terms of the dimensionless variables.

Within the lubrication approximation, Eqs. (1)–(3) become

$$\frac{\partial \tilde{u}_r}{\partial \tilde{y}} + \frac{\partial \tilde{u}_z}{\partial \tilde{z}} = 0, \quad (15)$$

$$\frac{\partial \tilde{p}}{\partial \tilde{y}} = 0, \quad (16)$$

$$\frac{\partial \tilde{p}}{\partial \tilde{z}} = 1 + \frac{\partial (\tilde{\mu} \partial \tilde{u}_z / \partial \tilde{y})}{\partial \tilde{y}}, \quad (17)$$

$$\frac{\partial^2 \tilde{T}}{\partial \tilde{y}^2} = 0. \quad (18)$$

In the above equations, inertial term has been neglected with  $\varepsilon \text{Re} \ll 1$ , where  $\text{Re} = \rho U_z H_0 / \mu_0$  and contains the velocity scale for the axial flow as described in Eq. (14). The convective heat transfer term has been neglected in the energy equation, Eq. (18) with  $\varepsilon \text{Pe} \ll 1$ , where  $\text{Pe} = U_z H_0 / \alpha$  is the Péclet number. Further, the solution is obtained with thin film approximation, i.e.,  $\varepsilon < 1$  [19]. The dimensionless form of no-slip and no-penetration boundary conditions at  $\tilde{y} = 0$  (cylinder surface) are

$$\tilde{u}_r = 0, \quad (19)$$

$$\tilde{u}_z = 0. \quad (20)$$

The nondimensional and simplified normal stress balance Eq. (9), tangential stress balance Eq. (10), and kinematic boundary condition Eq. (13) at  $\tilde{y} = \tilde{h}$  are

$$\tilde{p} = \text{Bo}^{-1} (\varepsilon^{-1} - \tilde{h} - \tilde{h}_{zz}), \quad (21)$$

$$\tilde{\mu} \frac{\partial \tilde{u}_z}{\partial \tilde{y}} = -\varepsilon \frac{\Delta T \gamma_T}{\mu_0 U_z} \frac{\partial \tilde{T}_i}{\partial \tilde{z}}, \quad (22)$$

$$\tilde{u}_r = \frac{\partial \tilde{h}}{\partial \tilde{t}} + \tilde{u}_z \frac{\partial \tilde{h}}{\partial \tilde{z}}. \quad (23)$$

Integrating energy balance Eq. (18) subject to the nondimensional constant surface temperature condition at  $\tilde{y} = 0$ ,

$$\tilde{T} = 1, \quad (24)$$

and energy balance at  $\tilde{y} = \tilde{h}$ ,

$$\frac{\partial \tilde{T}}{\partial \tilde{y}} = -\text{Bi} \tilde{T}, \quad (25)$$

yields an expression for the temperature profile across the film as

$$\tilde{T} = \frac{1 + \text{Bi}(\tilde{h} - \tilde{y})}{1 + \text{Bi}\tilde{h}}. \quad (26)$$

Interfacial temperature is therefore given by

$$\tilde{T}(\tilde{y} = \tilde{h}) = \tilde{T}^i = \frac{1}{1 + \text{Bi}\tilde{h}}. \quad (27)$$

The exponential viscosity model Eq. (4) after incorporating the temperature profile Eq. (26) is

$$\tilde{\mu} = \exp[-V(\tilde{T} - 1)] = \exp(v\tilde{y}), \quad (28)$$

where

$$v = \frac{V\text{Bi}}{1 + \text{Bi}\tilde{h}}, \quad (29)$$

and  $\tilde{\mu} = \mu/\mu_0$ . In the work of Leslie *et al.* [27], it was mentioned that the thermoviscosity number can vary from a small to a very large value, for example, for  $\Delta T = 25\text{K}$ ,  $|V| = 0.3825$  for acetic acid,  $|V| = 0.5225$  for silicone oil,  $|V| = 0.625$  for water,  $|V| = 2.5125$  for glycerol,  $|V| = 1$  for wax and slurry,  $|V| = 5$  for basaltic lava,  $|V| = 7$  for syrup, and  $|V| = 10\text{--}18$  for silicic lava. Therefore, a wide range of values of  $V$  is used in this study. In the experimental work of Zeng *et al.* [2] it was shown that Rayleigh-Plateau instability can lead to the heat transfer coefficient value of about  $100 \text{ W}/(\text{m}^2\text{K})$ . For a thin film of  $H_0 \sim 0.1 \text{ mm}$  (a cylinder radius of  $1 \text{ mm}$  implies  $\varepsilon = 0.1$ ) and  $k_{\text{th}} \sim 0.1 \text{ W}/\text{mK}$ ,  $\text{Bi} \sim O(0.1)$  can be obtained. In this study Biot number of up to  $O(1)$  has been used for all the results except for a few plots where Biot number has been varied up to  $O(10)$  following the previous theoretical studies [19,20,25]. Equations (15)–(17) are integrated subject to the boundary conditions given by the Eqs. (19)–(22) to obtain the velocity profile as

$$\tilde{u}_z = (1 + \tilde{h}_z/\text{Bo} + \tilde{h}_{zzz}/\text{Bo})v^{-2}\{\tilde{h} - 1 + [1 + (\tilde{y} - \tilde{h})]\exp(-v\tilde{y})\} - \text{Ma}T_z^i v^{-1}[1 - \exp(-v\tilde{y})]. \quad (30)$$

Using the velocity profile in Eq. (23) an equation governing the evolution of the interface shape is obtained as

$$\frac{\partial \tilde{h}}{\partial \tilde{t}} = -\frac{\partial}{\partial \tilde{z}} \int_0^{\tilde{h}} \tilde{u}_z d\tilde{y} = -\frac{\partial Q_z}{\partial \tilde{z}}, \quad (31)$$

TABLE I. Dimensionless parameters present in the governing equation.

Parameter	Representation	Physical meaning
Ma	$-\varepsilon\Delta T\gamma_T/\mu_0U_z$	Dimensionless surface tension gradient
Bo	$\rho gR^2/\varepsilon\gamma_0$	Ratio of gravitational force to surface tension force
Bi	$h_fH_0/k_{th}$	Ratio of convective heat transfer at the film surface to conduction across the film
V	$\lambda\Delta T/\mu_0$	Quantifies the effect of temperature on viscosity

where  $Q_z$  is the flux in the axial direction and is given by

$$Q_z(z, t) = -(1 + \tilde{h}_z/\text{Bo} + \tilde{h}_{zzz}/\text{Bo}) \left[ \frac{2\tilde{h}}{\nu^2} - \frac{\tilde{h}^2}{\nu} - \frac{2}{\nu^3} + \frac{2}{\nu^3} \exp(-\nu\tilde{h}) \right] - \text{Ma}T_z^i \left[ \frac{\tilde{h}}{\nu} - \frac{1}{\nu^2} + \frac{\exp(-\nu\tilde{h})}{\nu^2} \right]. \quad (32)$$

The key dimensionless parameters that appear in this model are summarized in Table I.

In Eq. (32), the first term on the right-hand side is the convective term due to mean flow under gravity, while the second and third terms correspond to the azimuthal and axial curvature effects respectively, and the fourth term accounts for the nonisothermal effects generated due to interfacial temperature gradient along the flow direction. In the following discussions, the tilde decoration on all the variables is dropped for the sake of convenience.

### B. Linearized model for small perturbations

The linear stability of the base state is explored by introducing the film thickness  $h(z, t) = h_0(z) + \delta h_1(z, t)$  in the evolution equation Eq. (31) where  $h_1(z, t)$  represents the perturbation to the film, and  $h_0(z) = 1$  is the base state profile where the flow profile is governed by the gravity and the opposing viscous stress. Collecting the  $O(\delta)$  terms the following linear equation is derived for the perturbation,

$$\frac{\partial h_1}{\partial t} + Ah_{1z} + Bh_{1zz} + Ch_{1zzzz} = 0, \quad (33)$$

where,

$$A = \frac{-1}{\nu_0^3} \left[ \left( \nu_0 + \nu_1 + \frac{3\nu_1}{\nu_0} \right) 2D + 3\nu_0\nu_1 \right], \quad B = \frac{\text{Ma}DT_1^i}{\nu_0^2} + C, \\ C = \frac{1}{\text{Bo}\nu_0^3} (2D + \nu_0^2), \quad D = 1 - \nu_0 - \exp(-\nu_0).$$

The interfacial temperature  $T^i$  in Eq. (27) and the parameter of the viscosity model  $\nu$  in Eq. (29) are dependent on the film thickness and therefore when the film is perturbed, these quantities get perturbed as

$$\nu = \nu_0(z) + \delta h_1(z, t)\nu_1(z), \quad T^i = T_0^i(z) + \delta h_1(z, t)T_1^i(z), \quad (34)$$

where

$$\nu_0 = \frac{V\text{Bi}}{(1 + \text{Bi})}, \quad \nu_1 = \frac{-V\text{Bi}^2}{(1 + \text{Bi})^2}, \quad T_0^i = \frac{1}{(1 + \text{Bi})}, \quad T_1^i = \frac{-\text{Bi}}{(1 + \text{Bi})^2}. \quad (35)$$

### III. LIMITING CASES

Some limiting models are discussed in this section.

#### A. Weak thermoviscous effect ( $V \rightarrow 0$ )

For the extreme limit of  $V \rightarrow 0$ , the governing equation, Eq. (31), becomes

$$\frac{\partial h}{\partial t} + \frac{\partial}{\partial z} \left[ (1 + h_z/\text{Bo} + h_{zzz}/\text{Bo}) \frac{h^3}{3} - \text{Ma} T_z^i \frac{h^2}{2} \right] = 0. \quad (36)$$

Continuing with this equation, the parameters in Eq. (33) become

$$A = 1, \quad B = -\frac{\text{Ma} T_1^i}{2} + \frac{1}{3\text{Bo}}, \quad C = \frac{1}{3\text{Bo}}, \quad D = 0. \quad (37)$$

These equations correspond to the case when the viscosity of the fluid is a constant (independent of temperature). This model is also valid for the case when the convective heat transfer is absent, i.e.,  $\text{Bi} = 0$ , except that for such a case, the thermocapillary term will also vanish. For  $\text{Ma} = 0$  or  $\text{Bi} = 0$  (equivalent to a nonheated surface) the analysis follows that of Duprat *et al.* [23] for thin films, except the length scales. In their study, the length scale for  $z$  direction was chosen so that the axial curvature is balanced by the gravity, and therefore obtained a parameter  $\beta_D$  that quantified the contribution of azimuthal curvature to the film dynamics with respect to the axial curvature. To balance the axial curvature term ( $h_{zzz}$ ) with gravity ( $O(1)$ ) in Eq. (36),  $z$  variable needs to be rescaled with  $L_z = \text{Bo}^{-1/3}$ . The azimuthal term becomes of order  $\text{Bo}^{-2/3}$ , and it is exactly equal to  $\beta_D$  as given by the expression in Eq. (1) in Duprat *et al.* [23]. Thus, for  $\text{Bo}^{-2/3} \ll 1$ , the contribution from the azimuthal curvature becomes negligible, and the equation for flow over a planar substrate [7,28] is obtained. This limit is valid for the model with the thermoviscous effect [Eq. (31)] as well.

#### B. Strong convection ( $\text{Bi} \gg 1$ )

For  $\text{Bi} \gg 1$ , the Marangoni stress disappears from the governing equation as  $T^i \rightarrow 0$ , and  $\nu \rightarrow V/h$  in Eq. (29). Therefore, the governing equation, Eq. (31) becomes,

$$\frac{\partial h}{\partial t} + f \frac{\partial}{\partial z} [(1 + h_z/\text{Bo} + h_{zzz}/\text{Bo}) h^3] = 0, \quad (38)$$

where  $f = [(V - 1)^2 + 1 - 2 \exp(-V)]/V^3$  is termed as fluidity as suggested by Wilson and Duffy [26]. Subsequently, the parameters in Eq. (33) become

$$A = 3f, \quad B = C = \frac{f}{\text{Bo}}. \quad (39)$$

It is noted that for a constant viscosity fluid,  $V \rightarrow 0$ , the fluidity parameter approaches a constant value,  $f \rightarrow 1/3$ . Thus, the model becomes similar to that presented in Sec III A except for the thermocapillary stress term. Thus, it can be seen that the convective heat transfer ceases to affect the thermoviscous terms for this limiting case.

### IV. TEMPORAL STABILITY ANALYSIS

Temporal stability analysis is performed by introducing normal mode perturbations of the form  $h_1 = \hat{h}_1 e^{i(kz - \omega t)}$  in the stability equation, Eq. (33), where  $\hat{h}_1$  is the amplitude,  $k$  is a real wave number and  $\omega$  is a complex frequency, i.e.,  $\omega = \omega_r^{\text{temp}} + i\omega_i^{\text{temp}}$ . Furthermore,  $\omega_i^{\text{temp}}$  quantifies the growth rate of the temporal evolution of the perturbation amplitude and  $\omega_r^{\text{temp}}$  quantifies the oscillation frequency of the perturbation. The system is temporally unstable if and only if  $\omega_i^{\text{temp}} > 0$ . The normal mode decomposition about the base profile  $h_0(z) = 1$  yields the following dispersion relation:

$$\omega = Ak + ik^2(B - Ck^2). \quad (40)$$

Therefore, the temporal growth rate is given by the expression

$$\omega_i^{\text{temp}} = Bk^2 - Ck^4, \quad (41)$$

which can be used to find the maximum temporal growth rate of the wave and is given by

$$\omega_i^{\text{max}} = \frac{Bk_{\text{max}}^2}{2}, \quad (42)$$

where  $k_{\text{max}} = \sqrt{B/2C}$ . The cutoff wave number,  $k_{\text{cutoff}}$  that delineates the stable and unstable regions in the  $k$  versus  $\omega_i^{\text{temp}}$  space is

$$k_{\text{cutoff}} = \sqrt{\frac{B}{C}} = \sqrt{1 + \frac{\text{MaBo}DT_1^i v_0}{(2D + v_0^2)}}. \quad (43)$$

From these expressions, it can be seen that even in the absence of heating, i.e.,  $\text{Ma} = 0$ , the system has a positive growth rate implying an unconditionally unstable system. This is due to the amplification of long-waves by the azimuthal curvature, leading to the well known Rayleigh-Plateau instability. As noted in many previous studies on the Rayleigh-Plateau instability, the cutoff wave number is simply  $k_{\text{cutoff}} = 1$  and is independent of the surface tension [8]. As shown in Sec. III B, even for strong convection, the thermocapillary effect disappears, and the Rayleigh-Plateau instability is recovered.

For the limiting case when the thermoviscous effect is negligible, the maximum growth rate is given by

$$\omega_i^{\text{max}}(V \rightarrow 0) = \frac{1}{3\text{Bo}} \left( 1 + \frac{3\text{Bo}}{2} \frac{\text{MaBi}}{(1 + \text{Bi})^2} \right)^2. \quad (44)$$

For an isothermal case,  $\text{Ma} = 0$ , or in the absence of convective heat transfer,  $\text{Bi} = 0$ , the growth rate of the disturbance on the gravity-driven film is governed by the curvature effects only as mentioned before, and hence is dependent only on Bond number. On a nonisothermal surface,  $\text{Ma} \neq 0$ , the presence of thermal convection,  $\text{Bi} \neq 0$  creates temperature gradient on the free surface with troughs closer to the cylinder temperature and crests closer to the ambient temperature. As mentioned earlier, the surface tension is a decreasing function of temperature. Thus, in the case when cylinder surface temperature is higher than the ambient temperature ( $T_s > T_\infty$ ), the troughs are hotter and therefore have lower surface tension than the crests. The thermocapillary stress is thus generated from the region of lower surface tension to the region of higher surface tension. This stress convects more liquid from the troughs to the crests leading to a larger growth rate of the instability for a heated substrate. The reverse argument holds true for the stabilizing effect of the thermocapillary stress on a substrate which is at a lower temperature than the ambient ( $T_s < T_\infty$ ). For a much larger convective heat transfer at the free surface,  $\text{Bi} \rightarrow \infty$ , the interfacial temperature gradient tends to zero as the entire free surface attains the ambient temperature, i.e.,  $T^i \rightarrow 0$ . Thus, the growth rate again becomes independent of the thermocapillary stress as is evident from Eq. (44).

Shown in Fig. 2(a) is the plot of the temporal growth rate as a function of wave number  $k$  for the case when thermocapillary stress is absent, i.e.,  $\text{Ma} = 0$ . In this figure, the  $V = 0$  case then corresponds to the isothermal flow (same as  $\text{Bi} = 0$ ), and shows the results for the Rayleigh-Plateau problem. For a heated cylindrical surface (i.e.,  $\text{Bi} \neq 0$  and  $V > 0$ ), the thermoviscous effect starts to stabilize the film due to a reduced velocity at the interface caused by an increase in viscosity at the free surface as a result of the convective cooling. The thermoviscous effect on the viscosity, and therefore on the unperturbed velocity profiles are shown in Fig. 3. The unperturbed velocity profile is simply due to the balance between the driving force, which is gravity and the opposing viscous stress. For a cylinder surface, which is cooler than the surrounding ( $V < 0$ ), the film interface temperature is higher due to the convective heating at the interface by the surrounding, leading to a destabilizing role of the thermoviscous effect. This mechanism of thermoviscous effect due to change in the fluid mobility close to the interface is consistent with the previous

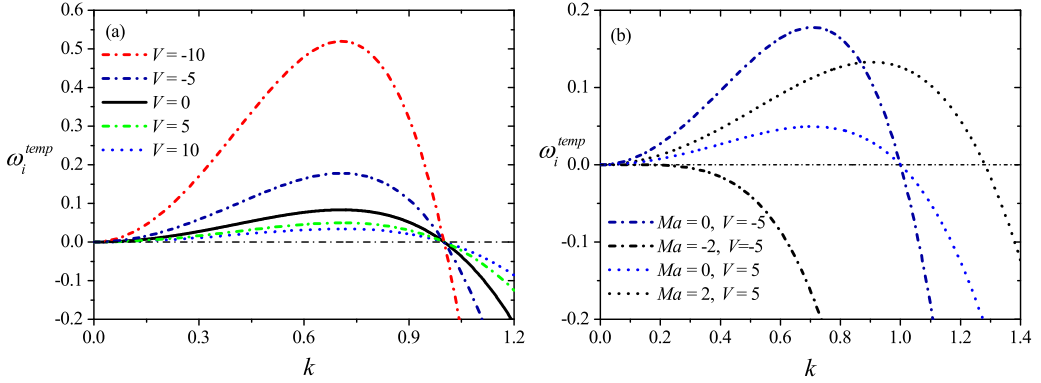


FIG. 2. (a). Effect of thermoviscosity number ( $V$ ) on the stability of the film in the absence of thermocapillary stress, i.e.,  $Ma = 0$ . (b) Effect of thermocapillary stress for a heated ( $V = 5$ ) and a cooled ( $V = -5$ ) substrate. For these results,  $Bi = 1$  and  $Bo = 1$ .

studies on thermoviscous fluid flow over a planar substrate [17,29,30]. The destabilizing effect of thermocapillary stress in the case of flow over a heated substrate is shown in Fig. 2(b). As mentioned earlier, thermocapillary stress acts from regions of lower surface tension to higher surface tension, pushing more fluid from the troughs to the crests of a wavy film leading to further destabilization of the film. By the same argument it is clear that the Marangoni stress tends to stabilize the film in case of a cooling substrate. For example, for the given parameter values,  $Ma = -2$  is sufficient to completely stabilize the film for all wave numbers. To further explore the role of thermocapillary stress, the leading growth rates  $\omega_i^{\text{max}}$  are plotted as a function of  $Ma$  for various values of  $V$  in Fig. 4. It is interesting to note that for  $V > 0$ ,  $k_{\text{cutoff}}$  increases as  $Ma$  increases indicating a broader unstable spectrum whereas it is reduced by an increase in  $V$ . In contrast, for  $V < 0$  and an increase in the thermocapillary action (indicated by an increase in the magnitude of  $Ma$ ), the unstable spectrum is reduced.

As shown in Fig. 3(a), an increase in  $V$  enhances the average viscosity of the film for a fixed value of Biot number. The role of Biot number appears in both thermocapillary as well as thermoviscous effects. The presence of Biot number affects the temperature  $T^i$  and, therefore, the temperature gradient  $T_z^i$  at the interface. For negligible convective heat transfer at the interface,  $Bi \rightarrow 0$  leads to  $T^i = 1$ , which implies that the interfacial temperature is uniform and is equal to the substrate temperature. As Biot number increases, the temperature gradient increases, and thus it enhances

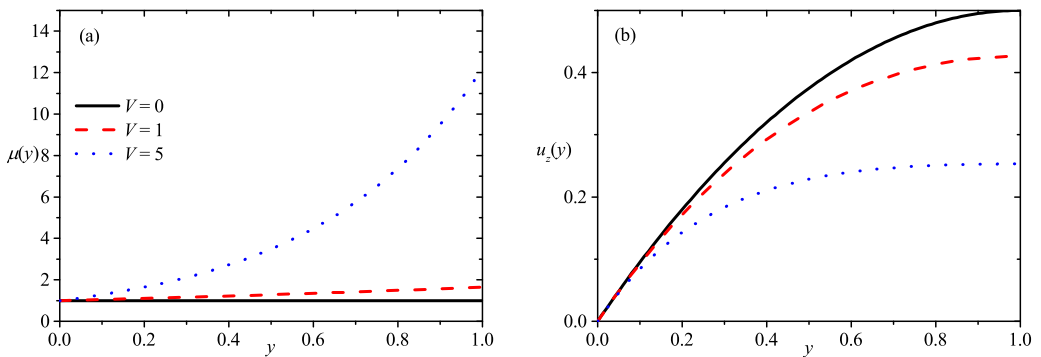


FIG. 3. (a) Viscosity variation along the radial direction for  $V = 0, 1$ , and  $5$ , and (b) corresponding (unperturbed) velocity profiles [Eq. (30)] with  $Bi = 1$ ,  $Bo = 1$ , and  $Ma = 0$ .

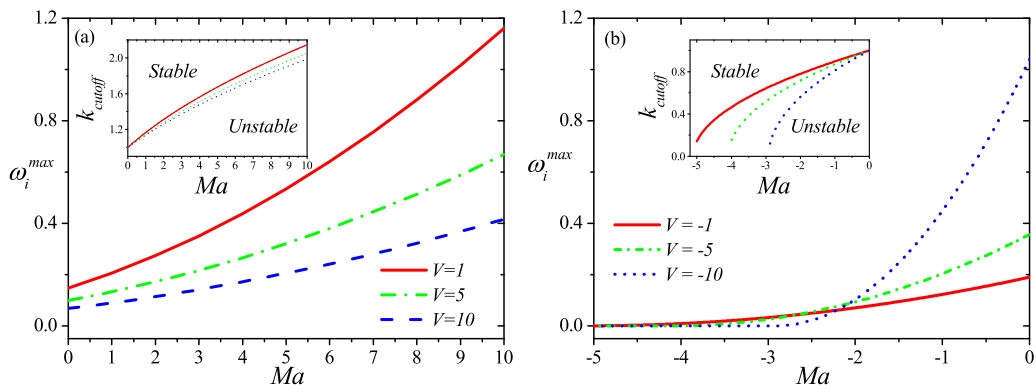


FIG. 4. Temporal growth rate of the most unstable wave  $\omega_i^{\max}$  and  $k_{\text{cutoff}}$  as a function of  $Ma$  for (a) heated ( $V > 0$ ) and (b) cooled ( $V < 0$ ) substrates. The other parameters are  $Bi = 1$  and  $Bo = 0.5$ .

the thermocapillary stress. For sufficiently large Biot number,  $Bi \rightarrow \infty$ , the interfacial temperature becomes  $T^i = 0$ , i.e., the interface attains the temperature of the surrounding. Thus, the effect of Biot number on thermocapillarity is nonmonotonic. However, temperature variation within the film due to a nonzero Biot number leads to the thermoviscous effect which is indicated by  $\nu$ . At moderate Biot number the thermoviscous effect is enhanced by an increase in the Biot number, and viscosity variation exists within the film. For a sufficiently large value of Biot number,  $\nu$  tends to a constant value and does not change further with  $Bi$ . For a heated substrate, an increase in the Biot number increases the average viscosity and hence stabilizes the film. The dual role of Biot number is indicated in Fig. 5 where  $\omega_i^{\max}$  is plotted versus  $Bi$  for various values of  $V$ . For  $V = 1$  the growth rate first increases and then decreases with  $Bi$  due to the nonmonotonic thermocapillary effect as explained above. The thermoviscous part dominates at larger values of  $V$ , stabilizes the flow and, therefore, the curve monotonically decreases. A similar effect is observed on  $k_{\text{cutoff}}$ , as shown in the inset of Fig 5.

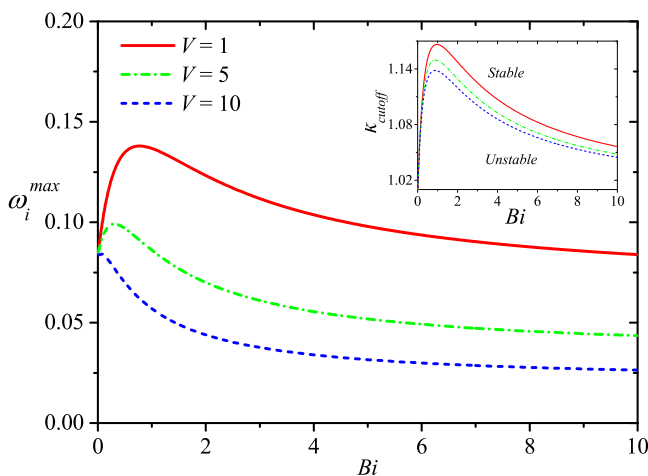


FIG. 5. Temporal growth rate of the most unstable wave,  $\omega_i^{\max}$  and  $k_{\text{cutoff}}$  plots as a function of  $Bi$  for different values of  $V$  and  $Ma = 1.5$   $Bo = 2$ .

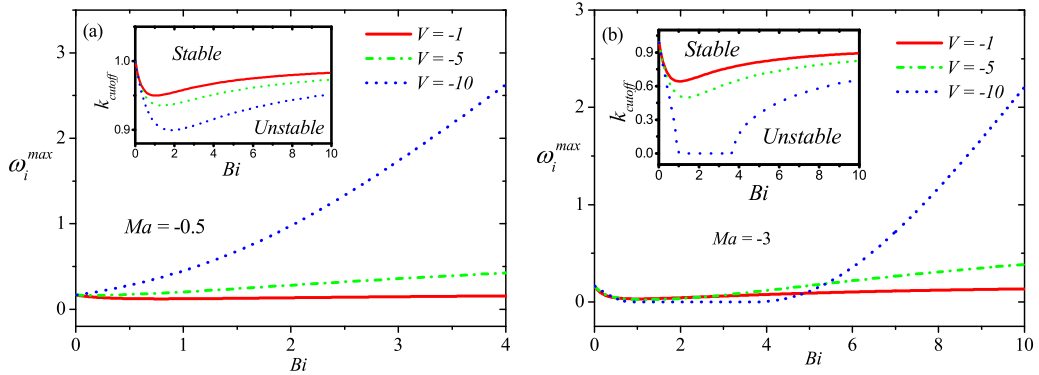


FIG. 6. Variation of  $\omega_i^{\max}$  and  $k_{\text{cutoff}}$  versus  $Bi$  (a)  $Ma = -0.5$ , and (b)  $Ma = -3$ , respectively, with  $Bo = 0.5$ .

For  $V < 0$  (colder solid surface), the film becomes less viscous as  $Bi$  increases due to enhanced convective heating at the interface. Thus, as shown in Fig. 6(a), the film becomes more unstable with an increase in Biot number at a moderate value of  $Ma$ . However, the thermocapillary effect is reversed compared to the  $V > 0$  case as the stress due to surface tension gradient moves fluid from crests to the troughs, making the film more stable. Thus, when the stabilizing action of Marangoni stresses are strong, as in the case of Fig. 6(b), growth rate ( $\omega_i^{\max}$ ) decreases for a range of  $Bi$  values and then increases. For a large magnitude of  $Ma$  and  $V$  there is a range of  $Bi$  for which zero maximum growth rate is observed, as shown in the figure before the effect of thermoviscosity results in increasing growth rates with  $Bi$ . The cutoff wave number,  $k_{\text{cutoff}}$  correspondingly varies with  $Bi$ .

The neutral stability curves that demarcate the stable and unstable regions are shown in Fig. 7 where the critical Marangoni number  $Ma_{\text{temp}}$ , beyond which the flow is temporally unstable, is plotted as a function of  $Bi$ . As mentioned earlier, the flow is always unstable for flow over a hotter cylinder. Therefore, such neutral curves are valid only for flow over a colder cylinder, which exhibits stable and unstable regions. The thermoviscous effects destabilize, and, however, the flow is stabilized by the Marangoni stresses. At lower values of  $Bi$ , the stable region expands with  $Bi$  as a result of the enhanced stabilizing effect of Marangoni stress, whereas, at higher values of  $Bi$ , the Marangoni stress reverses the role and, therefore, the stable region shrinks. At sufficiently large magnitudes of  $V$ ,  $Ma_{\text{temp}}$  becomes independent of  $Bi$  as indicated in Eq. (38).

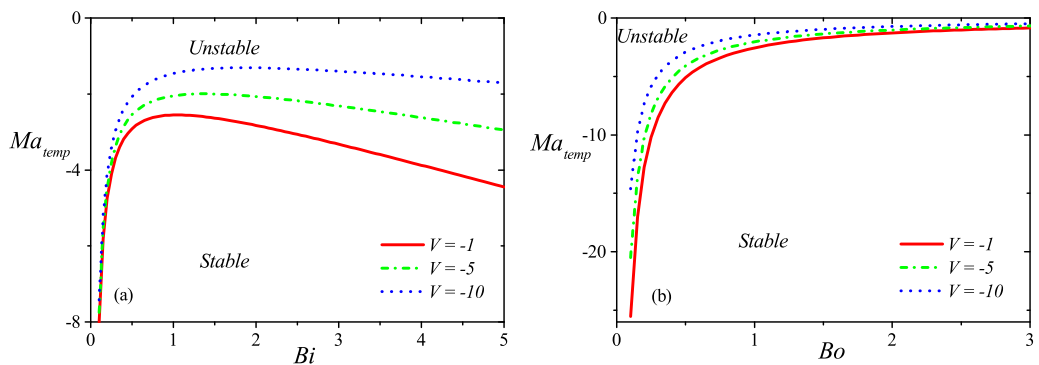


FIG. 7. Neutral stability curves illustrating stable and unstable regions in (a).  $Ma$ - $Bi$  parameter space for  $Bo = 1$ , and  $Ma$ - $Bo$  parameter space for  $Bi = 1$ .

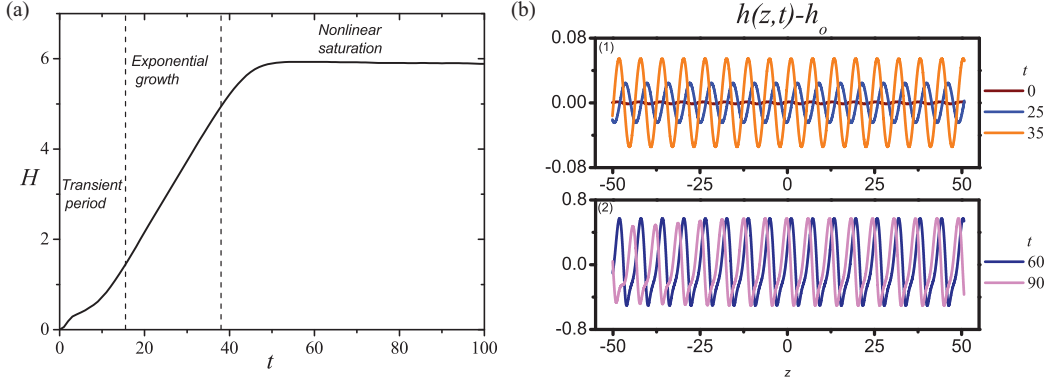


FIG. 8. (a) Different regions of the temporal evolution of perturbations for the real wave number  $k = 1.02$ , and  $\text{Ma} = 1.5$ ,  $\text{Bi} = 1$ ,  $\text{Bo} = 2$ ,  $V = 1$ . (b) Temporal evolution of perturbations generated by an initial sinusoidal disturbance introduced at  $t = 0$ . (1) Amplitude grows exponentially with time in the linear regime and (2) nonlinear saturation is achieved.

## V. NONLINEAR COMPUTATIONS FOR TEMPORAL GROWTH

Nonlinear evolution of a perturbation on the thin film was computed by solving Eq. (31) using the finite-element method with quadratic basis functions and implementing through COMSOL 5.0. A sinusoidal perturbation with a prescribed value of real wave number,  $k_r$  in the  $z$  direction was introduced at time  $t = 0$ . Calculations were carried out over the periodic domain of length  $2L = N(2\pi/k_r)$ , where  $N = 40$  was chosen, subjected to the following boundary conditions at the left boundary:

$$h(z = -L, t) = 1, \quad \frac{\partial h}{\partial z}(z = -L, t) = 0, \quad (45)$$

and the following soft conditions at the right boundary [28,31,32]:

$$\frac{\partial h}{\partial z}(z = L, t) = 0, \quad \frac{\partial^3 h}{\partial z^3}(z = L, t) = 0. \quad (46)$$

Absolute tolerance of  $10^{-9}$  was chosen for all the nonlinear computations.

The growth of the perturbation is quantified as

$$H = \ln \left[ \frac{\|h(z, t) - h_0(z)\|}{\|h(z, t = 0) - h_0(z)\|} \right], \quad (47)$$

where  $\|(\cdot)\|$  is the 2-norm and  $h_0(z) = 1$  is the base state profile. The time evolution of a sinusoidal perturbation is presented in Fig. 8(a) for the parameter values, as shown. There is a transient period ( $t < 15$ ), followed by the exponential growth ( $15 < t < 38$ ), and then the perturbation amplitude achieves nonlinear saturation beyond a certain time. The corresponding evolution of the film profile is presented in Fig. 8(b), wherein  $h(z, t) - h_0$  is plotted as a function of  $z$  at different time instants.

The temporal growth rate is extracted from nonlinear simulations by calculating the slope of the linear regime in  $H$  versus  $t$  curve. For example, the range  $15 < t < 38$  in Fig. 8 is used to compute the linear growth rate for the given set of parameter values. Thus,

$$\omega_{i,\text{NLS}}^{\text{temp}} \sim \frac{dH}{dt}. \quad (48)$$

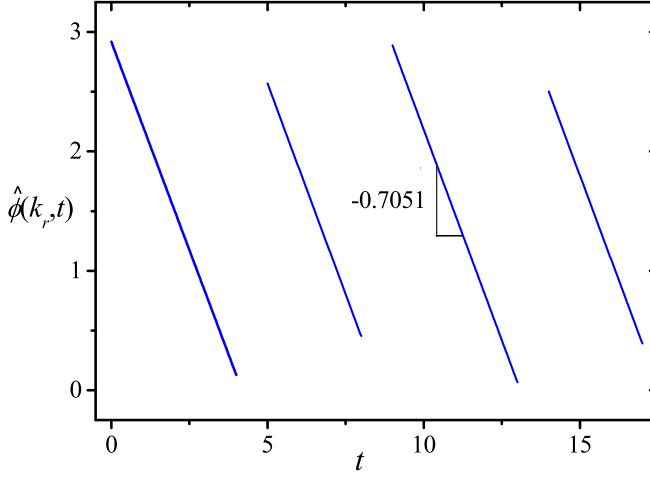


FIG. 9. Phase distribution versus time at  $k_r = 0.707$  for  $\text{Ma} = 0$ ,  $\text{Bi} = 1$ ,  $V = 0.01$ , and  $\text{Bo} = 0.5$ .

The imaginary part of the growth can be deduced from the nonlinear computations using the following methodology formulated by Delbende *et al.* [33]. The axial Fourier transform of  $h(z, t)$  is

$$\hat{H}(k_r, t) = \int_{-L}^L [h(z, t) - h_0(z)] e^{-ik_r z} dz.$$

A measure  $\hat{\phi}(k_r, t)$  of the associated phase distribution is conveniently chosen as [33]

$$\hat{\phi}(k_r, t) = \arg[\hat{H}(k_r, t)], \quad 0 \leq \hat{\phi}(k_r, t) \leq 2\pi. \quad (49)$$

The imaginary part of the complex wave frequency is then

$$\omega_r(k_r) = \frac{d\hat{\phi}(k_r, t)}{dt}, \quad (50)$$

and the descriptized form is

$$\omega_r(k_r) = \frac{\hat{\phi}(k_r, t_3) - \hat{\phi}(k_r, t_2)}{t_3 - t_2}. \quad (51)$$

Figure 9 displays the plot of  $\hat{\phi}(k_r, t)$  as a function of time. As noted by Delbende *et al.* [33], the phase function  $\hat{\phi}(k_r, t)$  is discontinuous every time it attains the value 0 or  $2\pi$ , so the time interval  $[t_2, t_3]$  is chosen in Eq. (51) such that the interval does not contain the points of discontinuity. The characteristic frequency of the wave oscillations thus recovered from the slopes of all the linear curves in Fig. 9 are exactly the same, so the specific choice of  $t_2$  and  $t_3$  does not matter.

A comparison between the linear stability results and the corresponding results from the nonlinear computations are presented in Table II for different parameter values. For the calculations of the growth rate and wave frequency,  $k_r = k_{r,\text{max}}$  (wave number of the fastest growing mode) was chosen for the initial sinusoidal perturbation. It can be seen that the agreement between the linear growth rate  $\omega_{i,\text{LSA}}^{\text{temp}}$  and that recovered from the nonlinear simulations  $\omega_{i,\text{NLS}}^{\text{temp}}$  are in an excellent agreement along with the wave frequency found from the linear ( $\omega_{r,\text{LSA}}^{\text{temp}}$ ) and nonlinear ( $\omega_{r,\text{NLS}}^{\text{temp}}$ ) analysis. The threshold wave number  $k_{\text{cutoff}}$  was found from the nonlinear simulations by varying the prescribed real wave number  $k_r$  in the imposed sinusoidal perturbation and tracking the transition from an unstable to a stable flow. The compliance between the two results indicates that the results from the temporal linear stability analysis are physically realizable.

TABLE II. Comparison of temporal growth rate of the most unstable wave,  $\omega_{i,\max}^{\text{temp}}$  and oscillation frequency of the perturbed wave  $\omega_r^{\text{temp}}$  determined from linear stability analysis (LSA) and retrieved from nonlinear numerical simulation results (NLS). These calculations were performed with  $\text{Bi} = 1$ .

Ma	Bo	V	$\omega_{i,\max,\text{LSA}}^{\text{temp}}$	$\omega_{i,\max,\text{NLS}}^{\text{temp}}$	$\omega_{r,\text{LSA}}^{\text{temp}}$	$\omega_{r,\text{NLS}}^{\text{temp}}$	$k_{\text{cutoff}}^{\text{LSA}}$	$k_{\text{cutoff}}^{\text{NLS}}$
0	0.5	0.01	0.1664	0.165	-0.706	-0.7051	1.00	0.99
1.5	2	1	0.1600	0.1573	-0.8868	-0.8864	1.44	1.43
3	4	10	0.1749	0.1739	-0.5483	-0.5482	2.12	2.11

## VI. SPATIOTEMPORAL STABILITY ANALYSIS

Temporal stability analysis determines whether the flow is stable or unstable. An unstable flow can be further divided into convectively and absolutely unstable flows. The system is said to be absolutely unstable if a local perturbation propagates both upstream and downstream, and invades the entire spatial domain. However, the local disturbance flows downstream from the source while growing in amplitude, and eventually leaves the domain in the case of a convectively unstable system. Therefore, spatiotemporal stability analysis needs to be accomplished to determine the occurrence of absolute and convective instabilities for the temporally unstable systems. The differential operator from the linear stability analysis represents a dispersion relation  $D(k, \omega) = 0$  in the complex space  $(k, \omega)$ . An impulse disturbance is imposed upon the operator and a corresponding Green's function,  $G(z, t)$ , gives the response. Subsequently, the long-time behavior of  $G(z, t)$  is analyzed along the rays along which  $z/t$  is constant. This quantity corresponds to the group velocity ( $V_g$ ) of the mode, i.e.,

$$\frac{d\omega}{dk}(k^*) = \frac{z}{t}. \quad (52)$$

The mathematical definition of convectively unstable flows is

$$\lim_{t \rightarrow \infty} G(z, t) = 0 \quad \text{along the ray } z/t = 0 \quad (53)$$

and for absolutely unstable flows

$$\lim_{t \rightarrow \infty} G(z, t) = \infty \quad \text{along the ray } z/t = 0. \quad (54)$$

According to the definitions Eqs. (53) and (54), absolute and convective instability depend on examining the long-time behavior of the wave number  $k^*$  observed along the ray  $z/t = 0$  at a fixed spatial location. This wave number  $k^*$  has, by definition, zero group velocity ( $V_g$ ), i.e.,  $V_g = d\omega/dk = 0$  and  $d^2\omega/dk^2 \neq 0$ , at the first-order saddle point. Briggs [34] criterion is then employed to find a pinch point in the complex  $k$ -plane, which is a crucial step in detecting the absolute and convective instabilities. Further, the cusp method of Kupfer *et al.* [35] is used to ascertain that the pinch point found using the Briggs criterion indeed corresponds to the group velocity associated with the spatiotemporal instabilities. Further theoretical details of the methods can be found in Ref. [36].

The procedure of the computations are presented now. Normal mode perturbations of the form  $\exp[i(kz - \omega t)]$  are introduced in the evolution model Eq. (31), where  $k = k_r + ik_i$  and  $\omega = \omega_r + i\omega_i$  are complex variables, and are related by the general dispersion relation,  $D(k, \omega) = 0$  as shown in Eq. (40). Spatial evolution of disturbances is taken into account by the complex nature of wave number where  $k_i$  represents the spatial development of the perturbation and  $k_r$  denotes the wave number of the perturbed wave. For a set of parameters, Brigg's method [34] is employed to calculate the saddle point in the  $k$  plane, as shown in Fig. 10(a). Further, the corresponding cusp-point formation in the  $\omega$  plane is shown in Fig. 10(b), as mentioned in the work of Kupfer *et al.* [35]. This figure shows an example of an absolute instability.

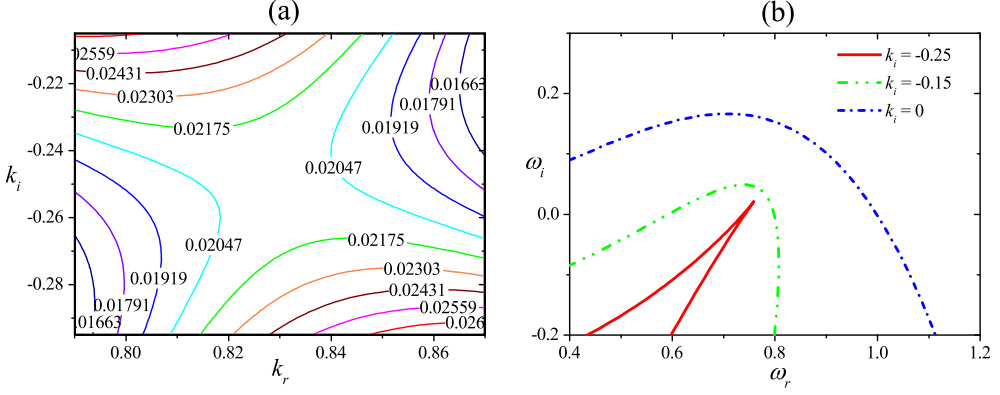


FIG. 10. (a) The contour map of  $\omega_i$  in  $k$  plane for the parameters  $\text{Ma} = 0$ ,  $\text{Bi} = 1$ ,  $\text{Bo} = 0.5$ , and  $V = 0.01$ . The saddle point forms at  $k_r = 0.8291$  and  $k_i = -0.2500$ , and  $\omega_i = 0.0208$ . (b) The corresponding cusp point in  $\omega$ -plane forms at  $\omega_r = 0.7598$  and  $\omega_i = 0.0208$  for  $k_i = -0.25$  and varying  $k_r$ .

The dispersion relation of Eq. (40) is rescaled by using  $\omega = \omega'(A^{4/3})/(3C)^{1/3}$  and  $k = k'(A/3C)^{1/3}$ . The rescaling transforms the dispersion equation into a standard form,

$$\omega' = k' + \frac{ik'^2}{3}(\beta - k'^2), \quad (55)$$

where  $\beta = B(9/A^2C)^{1/3}$ . This standard form of the dispersion relation has also been derived by Duprat *et al.* [23] in the context of an isothermal film flow on the exterior surface of a cylinder. The absolute growth rate,  $\omega'_i$  is evaluated following the Brigg's method [34] as illustrated in Fig 10(b). For absolutely unstable flows, the absolute growth rate  $\omega'_i > 0$  and for convectively unstable flows,  $\omega'_i < 0$ . Thus,  $\omega'_i = 0$  marks the transition from an absolutely unstable flow to a convectively unstable flow. By equating the absolute growth rate,  $\omega'_i$  at the saddle point to zero yields the critical value of  $\beta$ ,

$$\beta_{\text{critical}} \sim 1.507, \quad (56)$$

and equivalently,

$$B \left[ \frac{9}{A^2C} \right]^{\frac{1}{3}} = 1.507, \quad (57)$$

where  $A$ ,  $B$ , and  $C$  are given by Eqs. (33). The critical value of  $\beta$  obtained is consistent with that in the work of Duprat *et al.* [23]. Critical values of  $\text{Ma}$  are thus evaluated using

$$\text{Ma}_{\text{critical}} = \frac{v_0^2}{DT_1} \left( -C + 1.507 \left[ \frac{A^2C}{9} \right]^{\frac{1}{3}} \right). \quad (58)$$

It can be seen that for the limit  $V \rightarrow 0$ , Eq. (58) reduces to

$$\text{Ma}_{\text{critical}}^* \approx 1.005\text{Bo}^{-1/3} - (2/3)\text{Bo}^{-1}, \quad (59)$$

where  $\text{Ma}^* = \text{MaBi}/(1 + \text{Bi})^2$  is a composite Marangoni number. For a nonheated substrate ( $\text{Ma} = 0$ ), the condition on the Bond number for the transition from convective to absolute instability is obtained as  $\text{Bo} = 0.5403$ . The film is absolutely unstable for a smaller value of  $\text{Bo}$  than this critical value. This condition on Bond number is consistent with Eq. (3) in Ref. [23].

The neutral stability and marginal curves are demonstrated in Fig. 11. For the cooling case ( $V = -10$ ), the temporally unstable flow exhibits convective instability (in other words, the absolute

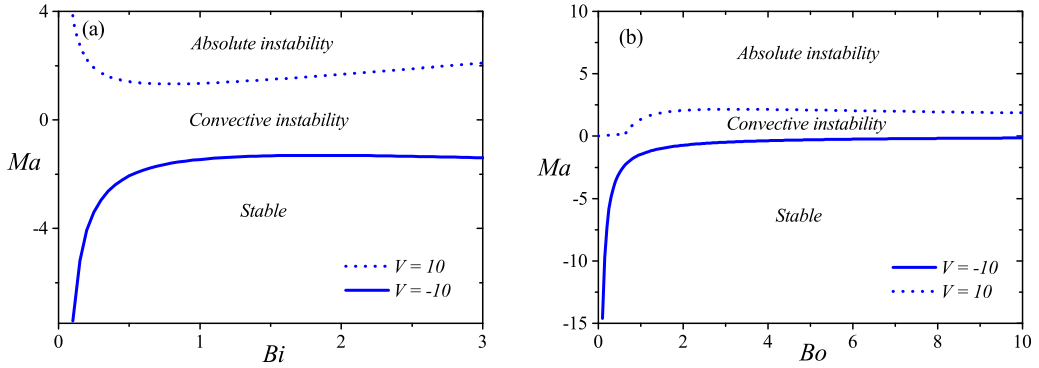


FIG. 11. Stable and convective/absolute unstable regions in the (a) Ma-Bi space for  $Bo = 1$ , and (b) Ma-Bo space for  $Bi = 1$  and  $V = -10, 10$ .

instability is absent), and thus the flow becomes convectively unstable at the onset of the instability. However, flow over a hotter cylinder ( $V = 10$ ) features both absolute and convective instabilities. The marginal curve demarcates the absolute and convective unstable flow regimes. Therefore, it can be concluded that the flow transits from convective to absolute instability regime when the Marangoni number is increased beyond a critical value.

Following the marginal curve sketched in Fig. 12(a), it is inferred that the flow is convectively unstable at smaller Bi for a wide range of Ma. As discussed earlier, when Bi is smaller the interfacial temperature gradient along the flow direction is smaller. Subsequently, the destabilizing thermocapillary stresses developed are also weaker. Thus, for the flow to exhibit absolute instability, the Marangoni force needs to be increased beyond a threshold value (higher Ma). As Bi increases, the flow transits to the absolute instability region on account of the elevated destabilizing role of Marangoni stress generated due to an increased interfacial temperature gradient. However, with further increase in Bi, interfacial temperature gradients are reduced, and consequently, the destabilizing Marangoni stress becomes weaker, in addition to enhanced viscosity of the film. Hence, the flow to become absolutely unstable larger values of Ma are required. Gravitational force drives the flow of liquid down the cylinder and is responsible for the instability getting convected away from the point of initiation. In the Ma-Bo parameter space Fig. 12(b), the flow exhibits convective instability at higher Bo due to the stronger effect of gravitational force. With the further increase in Bo, stabilizing role of streamwise curvature reduces and hence absolutely

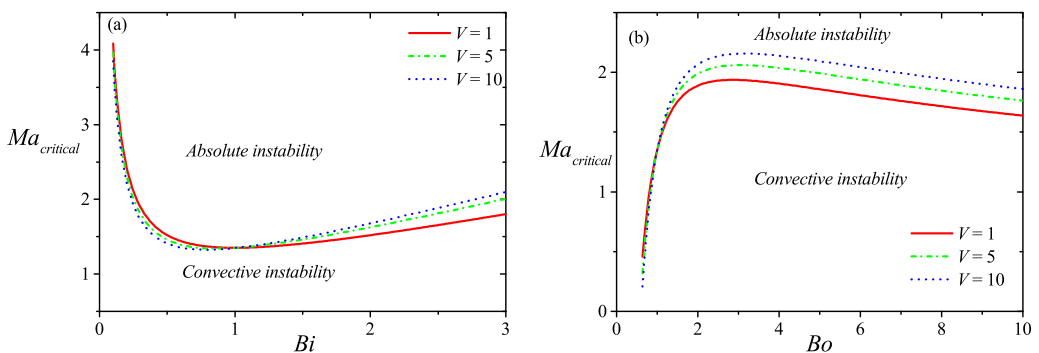


FIG. 12. Plot of neutral stability curves that mark the transition from absolute to convective instability (a)  $Ma_{critical}$  versus Bi at  $Bo = 1$ , and (b)  $Ma_{critical}$  versus Bo at  $Bi = 1$ .

unstable region increases. However, when the gravitational force is weaker at smaller  $Bo$ , the flow is absolutely unstable for arbitrary  $Ma$  and  $V$ .

In the work of Kliakhandler *et al.* [21], castor oil was used to study the formation of beads due to the instability of a thick film on a vertical wire. Castor oil can be a good model fluid to experimentally study the effect of thermoviscosity on the spatiotemporal stability of a thin film. For castor oil,  $\rho = 961 \text{ kg/m}^3$ ,  $\mu(T = 18^\circ\text{C}) = 1 \text{ cp}$ , and  $\gamma(T = 18^\circ\text{C}) = 0.031 \text{ N/m}$ . The gradient of surface tension with temperature is  $\gamma_T = -5 \times 10^{-5} \text{ N/m/K}$  [25]. The viscosity variation with temperature for castor oil [37] when fitted into the exponential model, as given in Eq. (4), yields  $\lambda = 0.121 \text{ Pa.s/K}$ . For an isothermal flow over a cylinder (e.g., a wire or a fiber of radius,  $R = 1 \text{ mm}$  and film-thickness of  $H = 0.1 \text{ mm}$ , the aspect ratio is  $\varepsilon = 0.1$ , and  $Bo = 3.04$ . The lubrication approximation is easily satisfied with  $\varepsilon Re \sim O(10^{-6}) \ll 1$  and  $\varepsilon Pe \sim O(10^{-3}) \ll 1$ . The Bond number for this flow configuration exceeds the critical value ( $Bo = 0.5403$ ), and therefore convective instability is expected. For a heated substrate with  $\Delta T = 40^\circ\text{C}$ , the parameters can be computed as  $V = 4.84$  and  $Ma = 2.12$ . For  $Bi = 1$ , the critical Marangoni number as given by Eq. (58) is found to be  $Ma_{\text{critical}} = 2.06$ . Since  $Ma > Ma_{\text{critical}}$ , the system now transitions into the absolute instability regime due to the thermal effects. Recently, liquid metals such as Gallium have been of interest due to their applications in stretchable and soft electronics, and instability generated on a flat substrate has been explored as a way to make interesting patterns relevant to the applications [38–40]. Therefore, instability over a cylindrical geometry may also lead to structures for such interesting applications. For liquid Gallium,  $\rho = 6048 \text{ kg/m}^3$ ,  $\mu(T = 350 \text{ K}) = 1.369 \text{ cp}$ , and  $\gamma(T = 350 \text{ K}) = 0.705 \text{ N/m}$  [41,42]. The Bond number  $Bo = 0.84$ , for the above-mentioned cylinder radius and film thickness, shows that the system is convectively unstable. With  $\gamma_T = -6.6 \times 10^{-5} \text{ N/m/K}$  and  $\lambda = 0.003 \text{ Pa s/K}$ , a temperature difference of  $\Delta T = 100^\circ\text{C}$  gives  $V = 0.22$  and  $Ma = 1.11$ . For  $Bi = 1$ , the system will transition into the absolute instability regime as  $Ma > Ma_{\text{critical}} = 1.08$ . In both the above analyses, the velocity scale due to natural convection was found to be at least two orders-of-magnitude smaller than that for the gravity-driven flow, and hence has been neglected.

## VII. NONLINEAR SPATIOTEMPORAL EVOLUTION OF DISTURBANCES

### A. Wave packet evolution

Nonlinear simulations of Eq. (31) were performed to study the nonlinear spatiotemporal dynamics of a localized impulse disturbance of the form

$$h(z, t) = 1 + 0.001 \exp\left(-\frac{z^2}{4}\right), \quad (60)$$

over a computational domain  $z \in [-L, L]$ . The domain size was chosen sufficiently large to accurately capture the spatial evolution of the disturbance. The boundary conditions are already discussed in Eqs. (45) and (46).

The wave packet evolves with time, as shown in Fig. 13(a), wherein the disturbance grows exponentially in the linear regime  $70 \leq t \leq 180$ . The instability is convected away from the source in the downstream direction, finally leaving the system in the undisturbed state. In contrast, for absolutely unstable flows, the disturbance spreads in the upstream as well as downstream direction; thus, the disturbance amplitude, outlined in Fig. 13(b), grows exponentially in the linear regime  $8 \leq t \leq 20$ , followed by the wave packet spreading over the computational domain in the interval  $20 \leq t \leq 120$ , and then the nonlinear saturation is attained by the instabilities. Shown in Fig. 14(a) are the film thickness profiles at different time instants for a convectively unstable flow corresponding to the growth curve in Fig. 13(a). The evolving film thickness profiles corresponding to the growth curve of Fig. 13(b) for the absolute instability are shown in Fig. 14(b).

The spatial and temporal progression of instabilities may also be followed on the waterfall curves [43] of Fig. 15, where the film thickness is sketched as a function of  $z$  at various time instants.

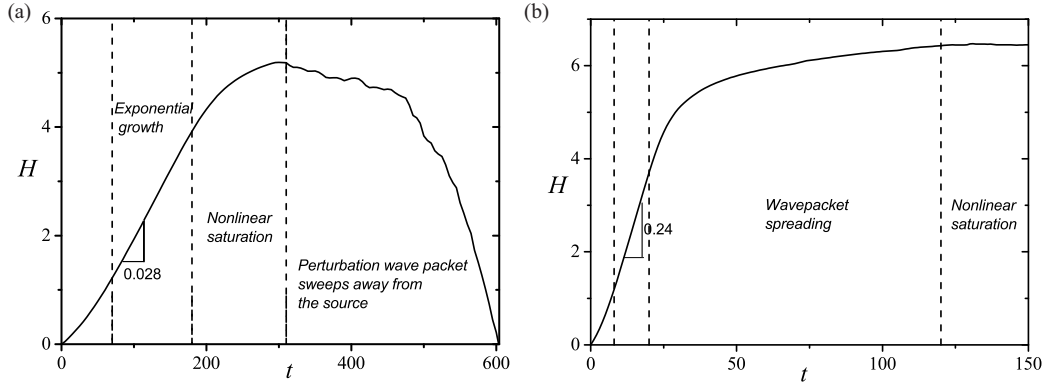


FIG. 13. Temporal evolution of the wave packet generated by an initial Gaussian perturbation for (a) convectively unstable flow, with the parameters  $Ma = 0.5$ ,  $Bi = 1$ ,  $Bo = 2$ ,  $V = 10$ , and (b) absolutely unstable flow, with the parameters  $Ma = 1.5$ ,  $Bi = 1$ ,  $Bo = 0.5$ ,  $V = 1$ .  $H$  is the amplification ratio as defined in Eq. (47).

The wave packet edges along which neutral waves propagate are also illustrated in Fig. 15. For convective instability, the front ( $V_+$ ) and rear ( $V_-$ ) end velocities are positive, and therefore the instability gets convected away from the point of initiation. In contrast, for the absolute instability,

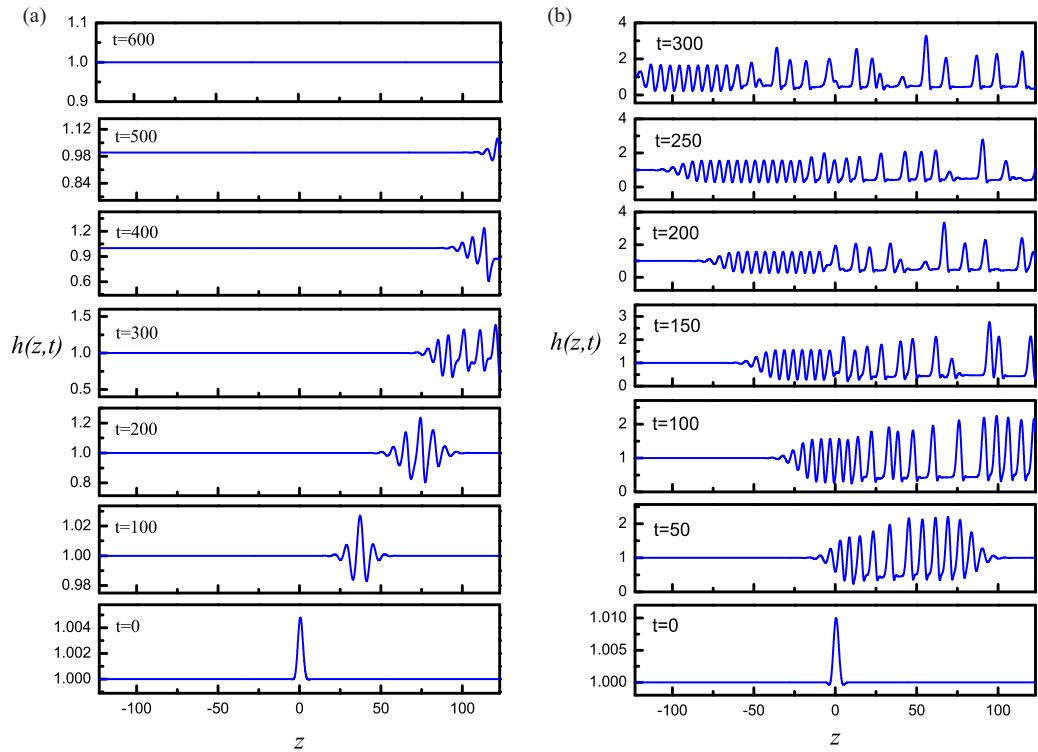


FIG. 14. (a) Convectively unstable flow at  $Ma = 0.5$ ,  $Bi = 1$ ,  $Bo = 2$ ,  $V = 10$ . (b) Absolutely unstable flow at  $Ma = 1.5$ ,  $Bi = 1$ ,  $Bo = 0.5$ ,  $V = 1$ .

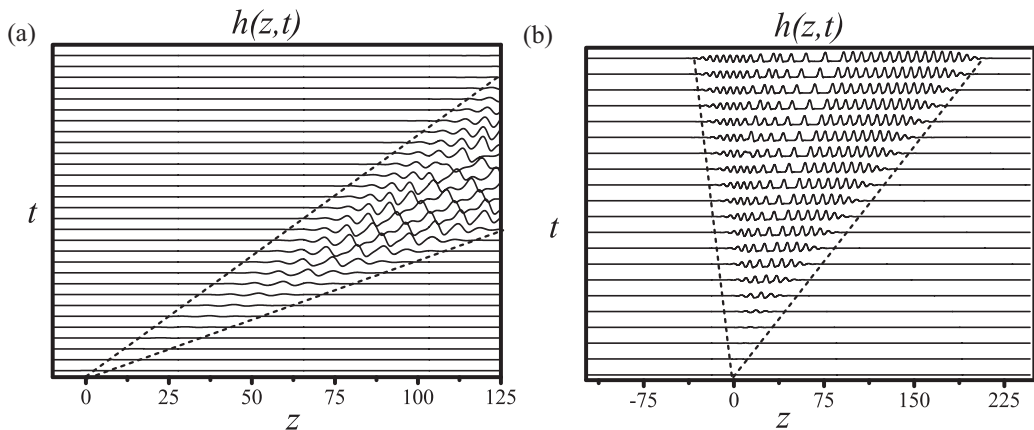


FIG. 15. Waterfall plot of film thickness  $h(z, t)$  in the  $(z, t)$  plane for (a) convectively unstable flow at  $Ma = 0.5$ ,  $Bi = 1$ ,  $Bo = 2$ ,  $V = 10$ , and (b) absolutely absolute flow at  $Ma = 1.5$ ,  $Bi = 1$ ,  $Bo = 0.5$ ,  $V = 1$ . The wave packet edges are also shown.

$V_+$  is positive and  $V_-$  is negative, and the initial localized instability eventually contaminates the entire flow.

### B. Spatiotemporal instability properties

In this section, the temporal and spatial evolution of the wave packet structure is investigated from nonlinear simulations, implemented in Sec. VII A. The nonlinear temporal evolution of the disturbance given by the initial condition Eq. (60) is shown in Fig. 13. For convective and absolute unstable flows, the perturbation amplifies exponentially in the linear regime,  $70 \leq t \leq 180$  and  $8 \leq t \leq 20$ , respectively. The wave packet characteristics are analyzed for this linear growth regime and compared with the linear spatiotemporal instability results. The numerical procedure discussed by Delbende *et al.* [33] is adopted to determine the spatiotemporal instability properties of the flow from the nonlinear computations.

The temporal growth rate observed along each ray is

$$\sigma(V_g) = \omega_i(V_g) - k_i(V_g)V_g. \quad (61)$$

The amplitude of the perturbation as a function of space and time is defined as

$$A'(z, t) = |h(z, t) - h_0|. \quad (62)$$

The amplitudes of the wave packet are enveloped by a Gaussian function,  $A(z, t)$ . This quantity  $A(z, t)$  has been shown to behave as

$$A(z, t) \propto t^{-1/2} \exp[\sigma(V_g)t]. \quad (63)$$

The temporal growth rate  $\sigma(V_g)$  along the ray  $z/t = V_g$  is calculated as follows:

$$\sigma(V_g) \sim \frac{d}{dt} \ln[t^{1/2}A(V_g t, t)], \quad (64)$$

and the discretized form is

$$\sigma(V_g) \sim \frac{\ln[A(V_g t_2, t_2)/A(V_g t_1, t_1)]}{t_2 - t_1} + \frac{\ln(t_2/t_1)}{2(t_2 - t_1)}, \quad (65)$$

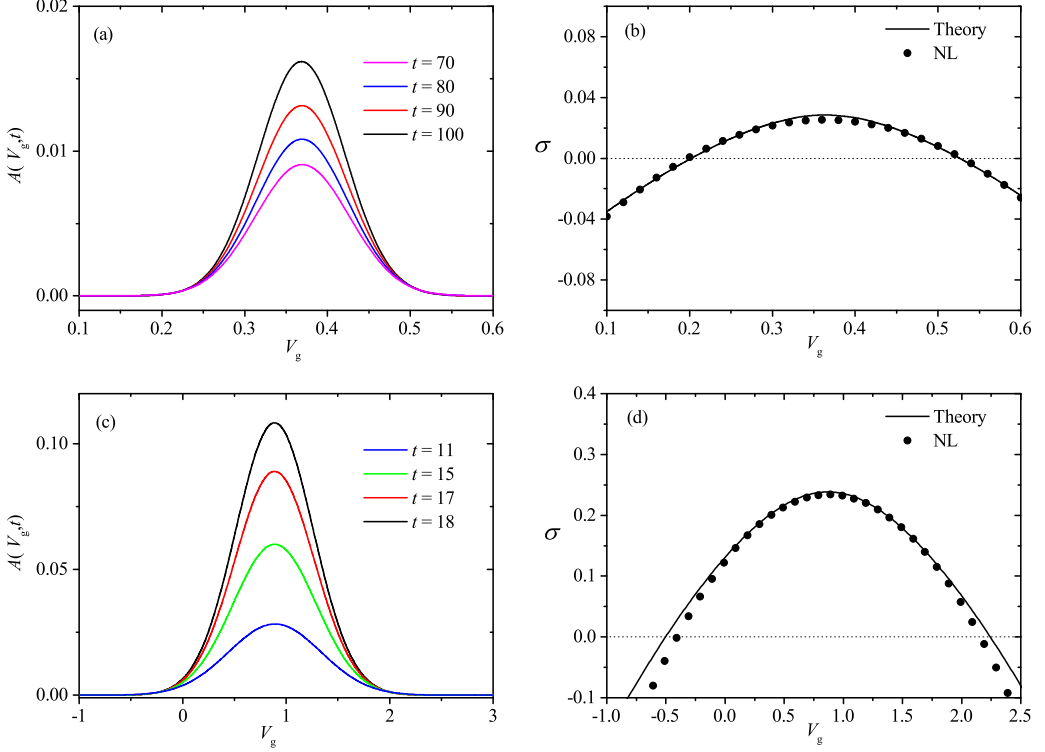


FIG. 16. Amplitude  $A(V_g, t)$  at various times for (a)  $Ma = 0.5$ ,  $Bi = 1$ ,  $Bo = 2$ ,  $V = 10$ , and (c)  $Ma = 1.5$ ,  $Bi = 1$ ,  $Bo = 0.5$ ,  $V = 1$ . Spatiotemporal growth rate  $\sigma(V_g)$  retrieved from nonlinear simulation results (NL) and theoretical calculations, (b) corresponding to (a), and (d) corresponding to (c).

where  $t_2 = 180$  (20) and  $t_1 = 70$  (8) for convective (absolute) instability. The imaginary part  $k_i$  of the wave number is evaluated using

$$k_i(V_g) = -\frac{d\sigma}{dV_g}(V_g). \quad (66)$$

The above equation avails the fact that the maximum achievable value of  $\sigma^{\max}(V_g)$  along any ray  $z/t$  coincides with the maximum temporal growth rate  $\omega_{i,\text{temp}}^{\max}$ , and that  $\sigma^{\max}$  is observed along the specific ray  $V_g^{\max} = d\omega_r/dk_i(k_i^{\max})$  [36]. The temporal growth rate,  $\omega_i(V_g)$ , is deduced from Eq. (61),

$$\omega_i(V_g) = \sigma(V_g) + k_i(V_g)V_g. \quad (67)$$

The amplitude of the perturbation  $A(z, t)$  versus  $V_g$  is shown in Fig. 16(a) for a convective instability and in Fig. 16(c) for an absolute instability. The associated spatiotemporal growth rates are illustrated on Figs. 16(b) and 16(d), as a function of the group velocity  $z/t = V_g$ . The two curves shown on each plot correspond to the theoretical results obtained using Eqs. (55) and (61), and the symbols correspond to the numerical results (NLS) retrieved from nonlinear simulations. The agreement between the theoretical and the nonlinear computation result is satisfactory.

The edge velocities are positive in Fig. 16(b), indicating that the flow is convectively unstable for the set of parameters studied. The  $\sigma^{\max}$  (Theoretical) coincides with the maximum temporal growth rate  $\omega_i^{\max}$ , and it occurs along the ray  $z/t = V_g^{\max}$ . The maximum attainable value of  $\sigma$  represents the dominant spatiotemporal mode over the spectrum of ray velocities and occurs when the ray velocity  $z/t$  equals the group velocity of the most unstable wave ( $\omega_i^{\max}$ ) for real  $k_r$ . Thus,  $V_g^{\max}$

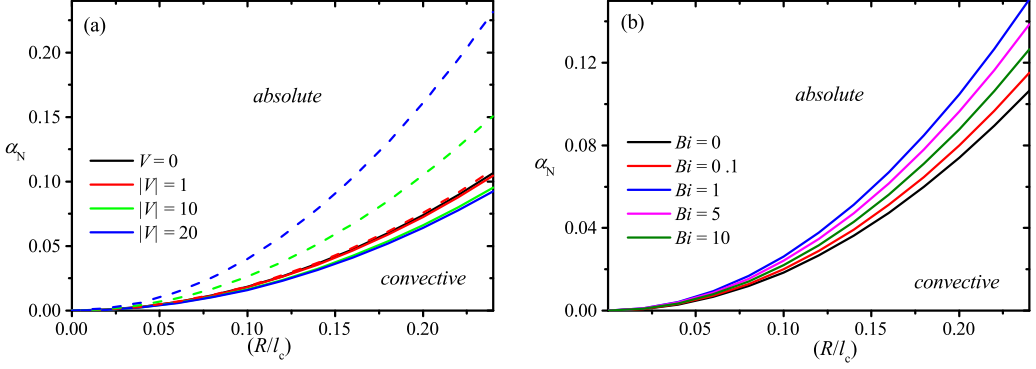


FIG. 17. Absolute and convectively unstable regions in the parameter space  $\alpha_N$  versus  $(R/l_c)$ , (a) for various values of  $V$  at  $Bi = 1$ , and (b) for various values of  $Bi$  at  $V = -10$ . In (a), the dashed lines correspond to  $V < 0$  and the solid lines correspond to  $V > 0$ . The thermocapillary stress is absent with  $Ma = 0$ .

denotes the group velocity of the dominant wave, and  $\sigma_{\max}$  signifies the temporal amplification of the wave packet. The temporal growth rate calculated from the plot of  $H$  in Fig. 13(a), that represents the perturbation amplification, also corresponds to the  $\omega_i^{\max}$ . The value is in agreement with the theoretical result within 7%. Shown in Fig. 16(d) is the growth plot for an absolutely unstable flow, where the front end velocity  $V_+$  is positive, and the rear end velocity  $V_-$  is negative. The absolute instability is governed by the wave with the group velocity  $V_g^{\max}$  and perturbation evolves with  $\sigma_i^{\max}$ , which matches with the value of  $\omega_i^{\max}$  [obtained from the linear slope in Fig. 13(b)] within 2%. Thus, it can be concluded that for an initial Gaussian disturbance, the dominant spatiotemporal mode governs the dynamics, implying that the perturbation amplifies temporally with  $\omega_i^{\max}$ .

### VIII. DISCUSSION

Detailed computational and theoretical studies on the transition between convective and absolute instabilities for flow down a vertical fiber was done by Duprat *et al.* [23]. They presented the absolute and convective instability regions in the parametric plane  $\alpha_N = H_0/R$  ( $= \varepsilon$  in this paper) versus  $R/l_c$ , where  $l_c = (\gamma_0/\rho g)^{1/2}$  is the capillary length. Note that the Bond number as defined in Table I is related to these parameters as  $Bo = (R/l_c)^2/\alpha_N$ . For the experimental work in Duprat *et al.* [23], silicone oil was used as the working fluid, and the radius of the fiber was varied from 0.23 to 1.5 mm. For a thin film  $\alpha_N < 1$ , the instability became absolute for  $\alpha_N > 1.85(R/l_c)^2$  (or, equivalently,  $Bo < 1/1.85 \approx 0.5405$ ). They further extended the model to account for the dynamics when drops become comparable to the radius of the fiber and the thin film approximation breaks down. In this section, the discussion is limited to the thin film assumption.

Ignoring the thermocapillary effect in Eq. (57), the expression for the critical Bond number for the transition between convective and absolute instabilities is given by

$$Bo = \frac{-1.62(2D + v_0^2)}{[(v_0 + v_1 + 3v_1/v_0)2D + 3v_0v_1]}, \quad (68)$$

which can be expressed in terms  $\alpha_N$  and  $(R/l_c)$  as

$$\alpha_N = -\frac{[(v_0 + v_1 + 3v_1/v_0)2D + 3v_0v_1]}{1.62(2D + v_0^2)}(R/l_c)^2. \quad (69)$$

For  $V \rightarrow 0$ , the expression reduces to the same condition as mentioned earlier from the work of Duprat *et al.* [23]. The parameter region is plotted in Fig. 17(a) where the effect of  $V$  on the critical curve between the convective and the absolute instability regions is shown. The dashed lines

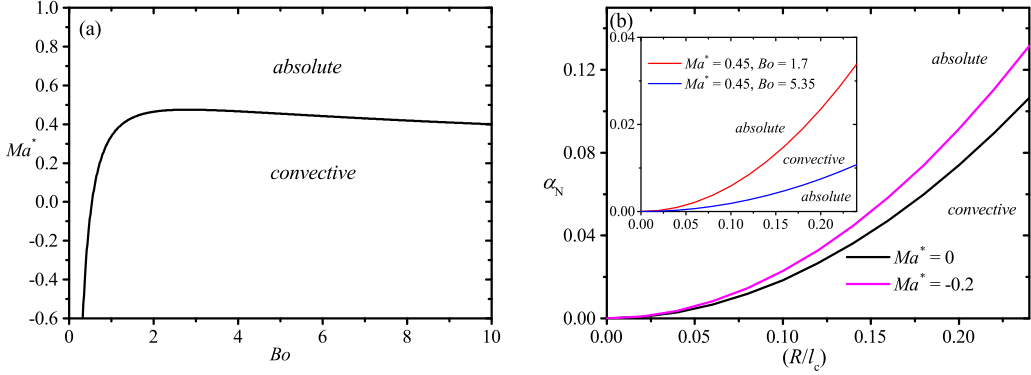


FIG. 18. Absolute and convectively unstable regions in the parameter space (a)  $Ma^*$  versus  $Bo$  and (b)  $\alpha_N$  versus  $(R/l_c)$  for  $Ma^* = 0$  and  $Ma^* = -0.2$ . Inset in (b) shows the parameter space for  $Ma^* = 0.45$ . Here  $V = 0$ .

correspond to  $V < 0$ , and the solid lines correspond to  $V > 0$ . Consistent with an earlier discussion on the magnitude of  $V$  for various fluids, a wide range of  $|V|$  is used in Fig. 17(a).

It is seen from Fig. 17(a) that for  $V > 0$ , an increase in the value of thermoviscosity number leads to an increase in the absolutely unstable region while shrinking the convectively unstable region. In contrast, for  $V < 0$  the absolutely unstable region shrinks. This indicates that a lower viscosity near the liquid-air interface as compared to the bulk makes the film convectively unstable. The role of Biot number is nonmonotonous as, shown in Fig. 17(b) for a constant thermoviscosity number,  $V = -10$ . As Biot number increases for  $V = -10$ , the absolute region shrinks, but beyond certain value, the critical curve again moves toward the  $Bi = 0$  curve. This is indicated in the expressions of  $\nu_0$  and  $\nu_1$  in Eq. (35) where for  $Bi \gg 1$ , the expressions become independent of the Biot number. At such large values, the entire film cross-section attains a constant temperature and hence the results follow an isothermal case. This result can also be verified by substituting the expressions of  $A$ ,  $B$ , and  $C$  in Eq. (39), valid for strong convection, into Eq. (57).

The effect of thermocapillary stress for a nonthermoviscous fluid,  $V = 0$ , is shown in Fig. 18(a) where the critical curve is plotted using Eq. (59). The curve delineates the parameter space for the absolute and convective instabilities. For a heated substrate ( $Ma^* > 0$ ), an absolute instability region expands with an increase in the strength of the thermocapillary stress. For a cooled substrate ( $Ma^* < 0$ ) only a narrow region exists for the absolute instability. The information is replotted in the parameter space of  $\alpha_N$  versus  $(R/l_c)$  in Fig. 18(b). For the cooled substrate, again the expansion of the convective region is indicated with respect to the isothermal case ( $Ma^* = 0$ ). For  $Ma^* > 0$ , at any constant value of  $Ma^*$ , there exist two values of  $Bo$  at which the transition from absolute to convective instability occurs. The two values can be found from Fig. 18(a) or by solving Eq. (59) for  $Bo$  at the constant value of  $Ma^*$ . The critical curves for such a case are plotted in the inset of Fig. 18(b) where  $Ma^* = 0.45$ . The transition occurs at two values of  $Bo$ ,  $Bo = 1.7$ , and  $Bo = 5.35$  as indicated in the figure. Therefore, a very narrow region is obtained in which convective instability is achieved outside which absolute region exists. This narrow region of convective instability keeps becoming narrower as  $Ma^*$  is increased further. It is interesting to note that beyond a critical point of  $Ma_{cp}^* = 0.4749$  (maxima of  $Ma^*$  versus  $Bo$  curve), the flow is absolutely unstable for all values of the Bond number. For a thermoviscous fluid, this critical point found from Eq. (58), is given by  $Ma_{cp}^* = -0.2374\nu_0^2 A/D$ , which is an increasing function of  $V$  ( $V > 0$ ), indicates that the critical Marangoni number increases with the thermoviscosity number. The values from this expression indeed match with the maxima of the critical curves shown in Fig. 12. Note that such a critical point does not exist for  $V < 0$  because, as can be seen from the nature of the curve in Fig. 11(b), the critical curve asymptotically approaches  $Ma = 0$ .

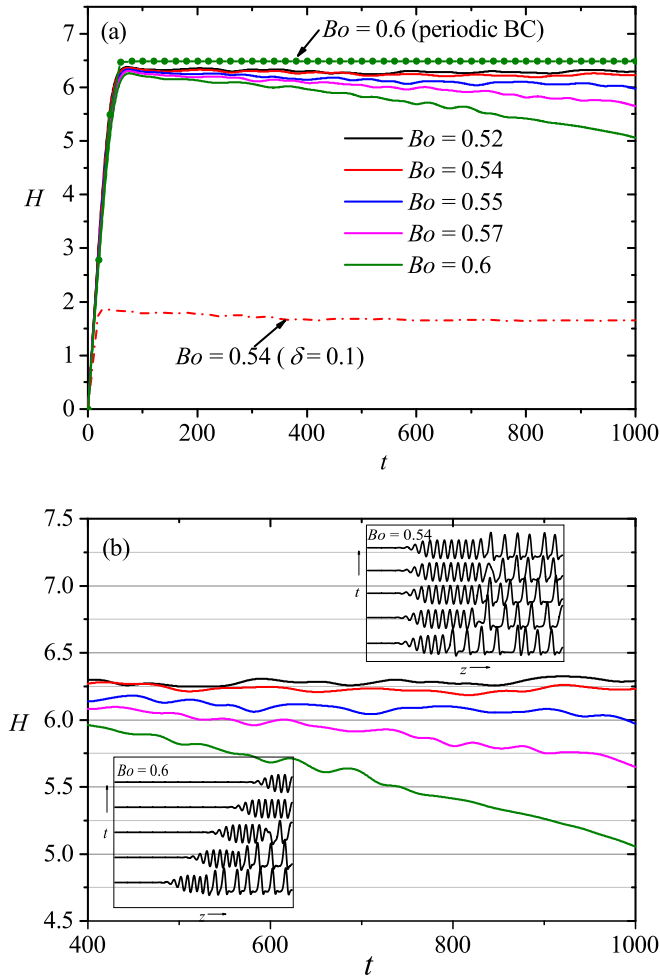


FIG. 19. (a) Nonlinear growth  $H$  versus time when  $\delta = 10^{-3}$ . One case with  $\delta = 0.1$  is also shown for  $Bo = 0.54$ . Also shown is a growth curve for  $Bo = 0.6$  with periodic boundary conditions. (b) Zoomed view of the decaying segment of the curves in (a). Inset also shows the nature of the evolving disturbance for an absolute instability ( $Bo = 0.54$ ) and a convective instability ( $Bo = 0.6$ ). The profiles shown are for  $t = 200, 400, 600, 800,$  and  $1000$ . The flow is considered to be isothermal here ( $Ma = V = 0$ ).

The nonmodal and nonlinear growth assumes importance in the study of thin liquid films [28,44]. These effects may also affect the transition between convective and absolute instability regimes [45]. Nonlinear computations are performed close to the transition curve to quantify this effect on the transition. The computational approach given in Sec. V is adopted in which a sinusoidal perturbation was imposed with a magnitude of  $\delta = 10^{-3}$ . The growth of the perturbation is plotted in Fig. 19 for  $Ma = 0$  and  $V = 0$ . As mentioned earlier, the critical parameter value for the transition from absolute to convective instability is  $Bo \simeq 0.5403$ . As can be noted from the figure, for all the values of  $Bo$  the perturbation grows at early times with the growth rate as predicted from the eigenvalues in Sec. IV. At later times, a convective instability leaves the domain [e.g., inset in Fig 19(b) for  $q = 0.6$ ], but, however, the absolute instability saturates to a self-sustained oscillatory mode [23,45]. This distinction is quantified by the slope of  $H$  versus  $t$ , as shown in Fig. 19(b). For  $Bo \geq 0.55$ , there is a negative slope indicating a convective instability. Due to the absence of a self-sustained disturbance, these instabilities were termed as globally stable in the review by Huerre

and Monkewitz [36]. However, for  $Bo \leq 0.54$ , a globally unstable mode was found, and the slope of  $H$  versus  $t$  was close to zero (for the computations a slope of  $10^{-5}$  was chosen as the cutoff). Thus, the nonlinear computations were able to capture the transition well. Close to the transition point, for  $Bo = 0.54$  growth of a large-amplitude perturbation of  $\delta = 0.1$  was also computed and is shown in Fig. 19(a). This perturbation attains the saturation earlier but yields the same exponential growth as well as the slope of the curve at later times as obtained for  $\delta = 10^{-3}$ . It must be noted that the periodic boundary conditions for such nonlinear computations cannot capture the transition because for the convective instability the waves leaving the domain downstream will enter the domain again from upstream due to the periodic conditions. One such case is illustrated for  $Bo = 0.6$  in Fig. 19(a) where periodic boundary conditions are employed for the nonlinear computation. The curve follows the same exponential growth regime at early times as obtained by the soft boundary conditions, but the decay at later times is not observed. The nonlinear computations were performed for several transition curves with the combined thermocapillary and thermoviscous effects as well with the approach mentioned, and again the transition values were found to be consistent with those predicted from the linear theory.

## IX. CONCLUSION

The gravity-driven coating flow of thin film outside a heated/cooled vertical cylinder was studied. Lubrication approximation was employed to derive the hydrodynamic equations governing the flow. The linear stability equations were derived to study the influence of various factors on the temporal stability. For an isothermal cylinder, the Rayleigh-Plateau exists, which is expectedly further augmented by the thermocapillary stress for a heated substrate. The thermoviscous effect tends to stabilize the flow on a heated cylinder due to larger viscosity at the liquid-air interface as compared to that at the solid surface. The scenario reverses on a cooled cylinder where the thermocapillary stress stabilizes the system, and the Rayleigh-Plateau instability can be suppressed completely for certain parameter values. Biot number (Bi) determines the relative effect of the thermocapillary stress and thermoviscous effect on the stability. As Biot number increases, the stabilizing effect of thermocapillary stress increases but then decreases for sufficiently large values of Bi. For small to moderate Bi the interfacial viscosity is smaller than that close to the substrate leading to a stable film. For much larger values of Bi, the liquid becomes less viscous making the thermoviscous effect more destabilizing. The Neutral stability curves indicate that this destabilizing effect of the thermoviscous effect is restricted to small magnitudes of the Marangoni number (Ma) and becomes stabilizing for large magnitudes of the Marangoni numbers. Bond number significantly affects these results and augments the effect of thermocapillarity on the temporal stability.

The occurrence of absolute and convective instabilities in the laboratory frame of reference was characterized by carrying out the spatiotemporal stability analysis. It was shown that the standard dispersion relation can be obtained by rescaling the variables, which is similar to that found in the work of Duprat *et al.* [23]. The saddle points were calculated using the Brigg's method [34], and the formation of cusp point in the  $\omega$  plane and the corresponding pinch point in the  $k$  plane were obtained by following the method outlined by Kupfer *et al.* [35]. The critical value of the composite parameter  $\beta$  that appeared in the standard form of the dispersion relation, was evaluated to study the transition from convective to absolute instability in the Ma-Bo and Ma-Bi parameter space. It was shown that for a cooled substrate, only convective instability exists for certain parameter values. An expression for the critical composite Marangoni number was found as a function of the thermoviscosity number beyond which the film was always absolutely unstable independent of the Bond number. This critical composite Marangoni number showed a monotonous increase with the thermoviscosity number.

Nonlinear simulations were performed to validate the linear analysis of the temporal and spatiotemporal dynamics. The numerical methodology suggested by Delbende *et al.* [33] was followed to retrieve the spatiotemporal properties, which were found to be in fair agreement with the theoretical results. Further, the transition between convective and absolute instability was

studied using sinusoidal perturbation as the initial condition, and a soft boundary condition at the downstream boundary (instead of the regular periodic condition, which is unable to capture the transition). The transition was found to be consistent with the linear theory even when the initial perturbation magnitude was 10% of the film thickness. The temporal growth rate and oscillation frequency were also retrieved from the nonlinear computations implying that the results of the eigenvalue analysis are physically determinant.

As far as we know, this is the first study of the flow of a thermoviscous fluid over a heated/cooled vertical cylindrical geometry. The instability of the isothermal flow leading to the breakup of the thin film into a series of droplets has been well understood. The challenge in such problems is that although the temporal instability leads to the pattern formation, which is desired for several applications as mentioned earlier, however, the instability needs to be further categorized as a convective or an absolute instability. In the case of a convective instability, though the pattern forms on the cylinder, it moves out of the domain with time, and the pattern does not exist. If the flow is absolutely unstable, then the pattern remains on the geometry (i.e., and shows well-behaved structures). Such a distinction between convective and absolute instabilities has been done both theoretically and experimentally by Duprat *et al.* [23]. Thus, the present work extends the understanding and provides a parameter regime in which absolute instability can be found for a nonisothermal application. The compliance between linear and nonlinear analysis suggests that the analytical expressions obtained from the linear stability analysis are capable of providing such parameter regimes, as illustrated in this study, thus leading to future experimental studies and applications.

- 
- [1] H. Chinju, K. Uchiyama, and Y. H. Mori, "String-of-beads" flow of liquids on vertical wires for gas absorption, *AIChE J.* **46**, 937 (2000).
  - [2] Z. Zeng, A. Sadeghpour, G. Warrier, and Y. S. Ju, Experimental study of heat transfer between thin liquid films flowing down a vertical string in the Rayleigh-plateau instability regime and a counterflowing gas stream, *Int. J. Heat Mass Transf.* **108**, 830 (2017).
  - [3] H. Ji, A. Sadeghpour, Z. Zeng, Y. S. Ju, and A. L. Bertozzi, Dynamics of thin liquid films on vertical cylindrical fibres, *J. Fluid Mech.* **865**, 303 (2019).
  - [4] H. Gau, S. Herminghaus, P. Lenz, and R. Lipowsky, Liquid morphologies on structured surfaces: From microchannels to microchips, *Science* **283**, 46 (1999).
  - [5] M. Binda, D. Natali, A. Iacchetti, and M. Sampietro, Integration of an organic photodetector onto a plastic optical fiber by means of spray coating technique, *Adv. Mater.* **25**, 4335 (2013).
  - [6] A. Kundan, T. T. T. Nguyen, J. L. Plawsky, P. C. Wayner Jr., D. F. Chao, and R. J. Sicker, Condensation on Highly Superheated Surfaces: Unstable Thin Films in a Wickless Heat Pipe, *Phys. Rev. Lett.* **118**, 094501 (2017).
  - [7] R. V. Craster and O. K. Matar, Dynamics and stability of thin liquid films, *Rev. Mod. Phys.* **81**, 1131 (2009).
  - [8] D. Quéré, Thin films flowing on vertical fibers, *Europhys. Lett.* **13**, 721 (1990).
  - [9] S. Kalliadasis, C. Ruyer-Quil, B. Scheid, and M. G. Velarde, *Falling Liquid Films* (Springer Science & Business Media, Berlin, 2011), Vol. 176.
  - [10] A. Frenkel, Nonlinear theory of strongly undulating thin films flowing down vertical cylinders, *Europhys. Lett.* **18**, 583 (1992).
  - [11] H.-C. Chang and E. A. Demekhin, Mechanism for drop formation on a coated vertical fibre, *J. Fluid Mech.* **380**, 233 (1999).
  - [12] S. Kalliadasis and H.-C. Chang, Drop formation during coating of vertical fibres, *J. Fluid Mech.* **261**, 135 (1994).
  - [13] V. Kerchman and A. Frenkel, Interactions of coherent structures in a film flow: Simulations of a highly nonlinear evolution equation, *Theor. Comput. Fluid Dyn.* **6**, 235 (1994).

- [14] L. Dávalos-Orozco and X. You, Three-dimensional instability of a liquid layer flowing down a heated vertical cylinder, *Phys. Fluids* **12**, 2198 (2000).
- [15] R. Liu and Z. Ding, Stability of viscous film flow coating the interior of a vertical tube with a porous wall, *Phys. Rev. E* **95**, 053101 (2017).
- [16] Z. Ding and T. N. Wong, Three-dimensional dynamics of thin liquid films on vertical cylinders with Marangoni effect, *Phys. Fluids* **29**, 011701 (2017).
- [17] A. R. Wazzan, T. Okamura, and A. Smith, The stability of water flow over heated and cooled flat plates, *J. Heat Transfer* **90**, 109 (1968).
- [18] C.-C. Hwang and C.-I. Weng, Nonlinear stability analysis of film flow down a heated or cooled inclined plane with viscosity variation, *Int. J. Heat Mass Transf.* **31**, 1775 (1988).
- [19] G. A. Leslie, S. Wilson, and B. Duffy, Thermoviscous coating and rimming flow, *Q. J. Mech. Appl. Math.* **65**, 483 (2012).
- [20] T. C. Kumawat and N. Tiwari, Hydrodynamic stability of thermoviscous liquid film inside a rotating horizontal cylinder: Heating and cooling effects, *Phys. Fluids* **30**, 032103 (2018).
- [21] I. Kliakhandler, S. H. Davis, and S. Bankoff, Viscous beads on vertical fibre, *J. Fluid Mech.* **429**, 381 (2001).
- [22] R. Craster and O. Matar, On viscous beads flowing down a vertical fibre, *J. Fluid Mech.* **553**, 85 (2006).
- [23] C. Duprat, C. Ruyer-Quil, S. Kalliadasis, and F. Giorgiutti-Dauphiné, Absolute and Convective Instabilities of a Viscous Film Flowing Down a Vertical Fiber, *Phys. Rev. Lett.* **98**, 244502 (2007).
- [24] R. Camassa, H. R. Ogrofsky, and J. Olander, Viscous film flow coating the interior of a vertical tube. Part 1. Gravity-driven flow, *J. Fluid Mech.* **745**, 682 (2014).
- [25] Z. Ding, R. Liu, T. N. Wong, and C. Yang, Absolute instability induced by Marangoni effect in thin liquid film flows on vertical cylindrical surfaces, *Chem. Eng. Sci.* **177**, 261 (2018).
- [26] S. Wilson and B. Duffy, Strong temperature-dependent-viscosity effects on a rivulet draining down a uniformly heated or cooled slowly varying substrate, *Phys. Fluids* **15**, 827 (2003).
- [27] G. A. Leslie, S. Wilson, and B. Duffy, Non-isothermal flow of a thin film of fluid with temperature-dependent viscosity on a stationary horizontal cylinder, *Phys. Fluids* **23**, 062101 (2011).
- [28] N. Tiwari and J. M. Davis, Nonmodal and nonlinear dynamics of a volatile liquid film flowing over a locally heated surface, *Phys. Fluids* **21**, 102101 (2009).
- [29] S.-M. Yih and R. C. Seagrave, Hydrodynamic stability of thin liquid films flowing down an inclined plane with accompanying heat transfer and interfacial shear, *AIChE J.* **24**, 803 (1978).
- [30] D. Goussis and R. Kelly, Effects of viscosity variation on the stability of film flow down heated or cooled inclined surfaces: Long-wavelength analysis, *Phys. Fluids* **28**, 3207 (1985).
- [31] C. Bielarz and S. Kalliadasis, Time-dependent free-surface thin film flows over topography, *Phys. Fluids* **15**, 2512 (2003).
- [32] H.-C. Chang, E. A. Demekhin, and S. S. Saprikhin, Noise-driven wave transitions on a vertically falling film, *J. Fluid Mech.* **462**, 255 (2002).
- [33] I. Delbende, J.-M. Chomaz, and P. Huerre, Absolute/convective instabilities in the batchelor vortex: A numerical study of the linear impulse response, *J. Fluid Mech.* **355**, 229 (1998).
- [34] R. J. Briggs, *Electron-stream Interaction with Plasmas* (MIT Press, Cambridge, MA, 1964).
- [35] K. Kupfer, A. Bers, and A. Ram, The cusp map in the complex-frequency plane for absolute instabilities, *Phys. Fluids* **30**, 3075 (1987).
- [36] P. Huerre and P. A. Monkewitz, Local and global instabilities in spatially developing flows, *Annu. Rev. Fluid Mech.* **22**, 473 (1990).
- [37] I. Abdelraziq and T. Nierat, Rheology properties of castor oil: Temperature and shear rate-dependence of castor oil shear stress, *J. Mater. Sci. Eng.* **5**, 1000220 (2015).
- [38] A. Leber, C. Dong, R. Chandran, T. D. Gupta, N. Bartolomei, and F. Sorin, Soft and stretchable liquid metal transmission lines as distributed probes of multimodal deformations, *Nat. Electron.* **3**, 316 (2020).
- [39] M. D. Dickey, Stretchable and soft electronics using liquid metals, *Adv. Mater.* **29**, 1606425 (2017).
- [40] T. D. Gupta, L. Martin-Monier, W. Yan, A. Le Bris, T. Nguyen-Dang, A. Gérald Page, K.-T. Ho, F. Yesilköy, H. Altug, Y. Qu, and F. Sorin, Self-

- assembly of nanostructured glass metasurfaces via templated fluid instabilities, [Nat. Nanotechnol.](#) **14**, 320 (2019).
- [41] M. J. Assael, I. J. Armyra, J. Brillo, S. V. Stankus, J. Wu, and W. A. Wakeham, Reference data for the density and viscosity of liquid cadmium, cobalt, gallium, indium, mercury, silicon, thallium, and zinc, [J. Phys. Chem. Ref. Data](#) **41**, 033101 (2012).
- [42] S. C. Hardy, The surface tension of liquid gallium, [J. Cryst. Growth](#) **71**, 602 (1985).
- [43] I. Delbende and J.-M. Chomaz, Nonlinear convective/absolute instabilities in parallel two-dimensional wakes, [Phys. Fluids](#) **10**, 2724 (1998).
- [44] P. J. Schmid and D. S. Henningson, *Stability and Transition in Shear Flows* (Springer Science & Business Media, Berlin, 2012), Vol. 142.
- [45] J.-M. Chomaz, Global instabilities in spatially developing flows: Nonnormality and nonlinearity, [Annu. Rev. Fluid Mech.](#) **37**, 357 (2005).